

THESIS ON MECHANICAL ENGINEERING E99

**Measurement Methods with 3D Coordinate
Measuring Machine and Improved
Characterization Setup for
Detector Performance**

KLODIAN DHOSKA

TUT
PRESS

TALLINN UNIVERSITY OF TECHNOLOGY
Faculty of Mechanical Engineering
Department of Mechatronics

Dissertation was accepted for the defense of the degree of Doctor of Philosophy in Engineering on May 4, 2016.

Supervisor: Prof. Toomas Kübarsepp,
Department of Mechatronics, Tallinn University of
Technology

Opponents: Dr. Ing. Marek Šmíd,
Head of Department of Radiometry and Photometry, Czech
Metrology Institute (NMI), Czech

DSc. Mart Noorma,
Vice Rector for Academic Affairs, University of Tartu, Estonia

Defense of the thesis: June 16th 2016 at 13:00
Tallinn University of Technology
Ehitajate tee 5, Tallinn, Estonia

Declaration:

Hereby I declare that this doctoral thesis, my original investigation and achievement, submitted for the doctoral degree at Tallinn University of Technology, has not been submitted for any other degree.

/Klodian Dhoska/



European Union
European Social Fund



Investing in your future

Copyright: Klodian Dhoska, 2016
ISSN 1406-4758
ISBN 978-9949-23-957-3 (publication)
ISBN 978-9949-23-958-0 (PDF)

MEHCHANOTEHNIKA E99

**Mõõtemetodid detektori toimimise
iseloostamiseks 3D-koordinaat-
mõõtemasina ja arendatud mõõteskeemiga**

KLODIAN DHOSKA

CONTENTS

ABBREVIATIONS	6
SYMBOLS.....	7
INTRODUCTION	9
1. LITERATURE REVIEW	12
1.1 Overview of 3D CMM Metrology	12
1.2 SPAD detector for imaging purposes.....	16
2. ANGLE MEASUREMENT METHOD FOR UNCERTAINTY EVALUATION OF COMPLICATED GEOMETRICAL OBJECTS BY USING THE COORDINATE MEASURING MACHINE	20
2.1 Measurement instrument and methodology	20
2.2 Measurement model	24
2.3 Evaluation of measurement uncertainty and research results	25
3. ALIGNEMENT POSITION METHOD FOR Si-SPAD DETECTOR CALIBRATION PROCESS AND INVESTIGATION OF THE DETECTION EFFICIENCY HOMOGENEITY.....	30
3.1 Measurement setup and methodology.....	30
3.2 Si-SPAD detector alignment.....	33
3.3 Research results.....	35
3.3.1 Results of Si-SPAD alignment position	35
3.3.2 Homogeneity studies.....	42
4. HIGH-ACCURACY FILTER MEASUREMENT METHOD FOR CALIBRATION OF THE DETECTION EFFICIENCY OF Si-SPAD DETECTOR.....	47
4.1 Measurement methodology.....	47
4.2 Measurement model	51
4.3 Uncertainty evaluation in the detection efficiency and research results	52
5. CONCLUSIONS.....	56
REFERENCES	58
LIST OF PUBLICATIONS	62
OTHER PUBLICATIONS	63
ACKNOWLEDGEMENTS	65
ABSTRACT.....	66
KOKKUVÕTE	67
ELULOOKIRJELDUS	68
CURRICULUM VITAE.....	70

ABBREVIATIONS

CAD	Computer Aid Manufacturing
CMM	Coordinate Measuring Machine
CMOS	Complementary Metal Oxide Semiconductor
EMRP	European Metrology Research Programme
GUM	Guide to the Expression of Uncertainty in Measurement
ISO	International Organization for Standardization
PDM	Micro Photon Device
PTB	Physikalisch-Technische Bundesanstalt, National Metrology Institute of Germany
RSD	Relative Standard Deviation
SI	Le Système International d'Unités, International System of Units
SIQUTE	Single-photon sources for quantum technologies
Si-SPAD	Silicon Single Photon Avalanche Diode
SPAD	Single Photon Avalanche Diode
SPCM-AQR	Single Photon Counting Module
SPD	Single Photon Device
TOF	Time of Flight

SYMBOLS

a	height of the curve peak
A_1	amplification factor
A_2	amplification factor
A_3	amplification factor
b	center position of the peak
c	speed of light
c_i	sensitivity coefficients for all input quantities
d_1, d_2	beam diameters
E_G	parameter due to the specification of 3D CMM
E_k	parameter due to the specification of 3D CMM
f	objective focal plane
$f(Y)$	function of the form
F_{Filt}	factor that uses two filters
h	Planck constant
k	coverage factor
L	distance between two points
n	independent observations
N_{center}	Si-SPAD count rate at the center position
N_{x_i, y_j}	Si-SPAD counts for the (x, y) -position
Q_1	signal of the Si-diode attached to the integrating sphere
Q_2	signal of the Si-diode attached to the integrating sphere
Q_3	signal of the Si-diode attached to the integrating sphere
Q_4	ratio of the counter and the monitor detector signal
R	resolution of the 3D CMM
s_{mon}	signal of the monitor detector
S_i	modified irradiance distribution over a scanning region
S_{Si}	spectral responsivity of the integrating sphere with the attached Si-Diode
T_{Combined}	filter transmission of combined filter
$T_{\text{Filter2}}, T_{\text{Filter3}}$	transmissions of each individual filter
U	expanded uncertainty
$u(\delta x_i)$	standard uncertainty of the input quantities of 3D CMM
$u(\delta \eta_{\text{Ffilt}})$	standard uncertainty due to the correction factor that uses two filters
$u_c(y)$	combined uncertainty
x	measured value
X	coordinative measuring in X-direction
x_{21}	distance between two points in X-direction
x_{center}	center position of the detector in X-direction
x_{diameter}	beam diameter in X-direction
x_i	observed readings
x_m	mean value of the readings

y	estimate of the output quantity
Y	coordinative measuring in Y-direction
Y	scanning positions in Y-directions
y_{21}	distance between two points in Y-direction
y_{center}	center position of the detector in Y-direction
y_{diameter}	beam diameter in Y-direction
Z	coordinative measuring in Z-direction
Z_1, Z_2	beam distances in Z-direction
z_{21}	distance between two points in Z-direction
δx_{cal}	correction from calibration of machine
δx_{L}	correction from distance between two points
δx_{probe}	correction from probing error
δx_{read}	correction from reading of indication
δx_{rep}	correction from repeatability
$\delta \eta_i$	corrections from all input quantities in the detection efficiency of Si-SPAD detector
η	detection efficiency of Si-SPAD detector
λ	wavelength
σ	standard deviation of the count rate

INTRODUCTION

In the modern automation technologies, the role of mechatronic systems in industrial product development processes is crucial. Simultaneously, mechatronic systems require adequate service techniques. A fundamental part of many mechatronic systems is a measurement system and a measurement procedure; thus, metrology as the science of measurement is omnipresent in today's society [1, 2]. In many industrial systems, all activities connected with measurement and testing functions for providing the quality of the product are focused in the production metrology, as reported in [3]. The main function of production metrology is to record an object's quality criteria measurements. An object of measurement will be often a workpiece; however, it can also be a tool, a machine or even a measuring device within the scope of test equipment monitoring [3].

3D Coordinate Measuring Machines (CMMs) and Machine Vision, as parts of mechatronic systems used in a broad range of application areas, have played an important role in many industrial manufacturing processes [4, 5].

According to leading experts in Europe, it is expected that the 21st century will be the century of the photon [6]. The emerging technologies in photonics need accurate optical power measurement covering conventional detectors as well as advanced single photon measurement devices. This sets higher challenges to metrology institutions to develop improved and simplified traceability methods to meet these demands, as the annual market growth rate of photonics in Europe is about 8%.

To realize a well-functioning detector for photonics, the opto-mechanical items should be carefully designed and thoroughly measured to fit the desired purpose. With an increasing demand of complex detector design, challenges for already manufactured mechanical parts are also increasing. To meet the needs for accurate measurements of complicated objects, 3D CMMs can be used. However, 3D CMMs have not been extensively used in optical radiometry community, mainly owing to lack of routine and reliable measurement methods for relatively small mechanical parts.

When the detector is realized, its electro-optical properties have to be characterized traceable to SI units. This is important to ensure the accuracy of the 3D imaging used in vision technologies whose area is gradually expanding towards few and single photon devices (SPD) to enable better imaging accuracy, higher data flow and to secure the communication. Amongst the other features, the accurate knowledge of SPD detection efficiency can increase image reliability and quality, and secure communication in machine vision channels.

In the last decade, much research has been focused on the angle measurement methods for regular geometric objects by using 3D CMMs. In manufactured mechanical parts, the angle measurement method for complicated geometrical objects such as photodetectors by using 3D CMMs has attracted major research interest. The advantage of the angle measurement method in complicated

geometrical objects by applying 3D CMMs instruments over the other dimensional measuring instruments lies in reliability and accuracy.

Another important aspect in this thesis research is how to improve accuracy of imaging in the vision technologies. Many researchers have focused on the integration of the Silicon Single Photon Diode (Si-SPAD) detectors to Complementary Metal Oxide Semiconductor (CMOS) and the Time of Flight (TOF) technique for the purpose of accurate imaging. The need for metrological characterization of the Si-SPAD detectors as a key component usable to ensure imaging accuracy has increased interest in research in this dissertation.

This study is composed of two main parts: the first part focuses on a thorough state-of-the-art in metrology used for 3D CMM by measuring complicated geometrical object such as optical photodetector. The second part of the study focuses on characterizations of the Si-SPAD detectors as a key component used for accuracy of imaging purposes in vision technologies.

Furthermore, it is obvious that from a metrological point of view, any significant measurement realized in this study is traceable to SI units and is accompanied with a stated measurement uncertainty.

The Main Objectives of the Thesis

The two main objectives of the thesis are as follows. Firstly, the objective is to elaborate a reliable and accurate angle measurement method for complicated geometrical objects by using 3D CMMs. The second objective is related to the metrological characterization of the Si-SPAD detectors. The tasks to be solved are as follows:

- Development of the angle measurement method and uncertainty estimation for complicated geometrical objects by using a 3D Coordinate Measuring Machine (CMM)
- Development of a high accuracy method for the characterization of Silicon Single photon avalanche diode (Si-SPAD) detectors used for imaging purposes that consists of:
 - a. Methodology for investigation of the quantum detection homogeneity of Si-SPAD detectors
 - b. Achievement of lower uncertainty in determination of the detection efficiency of Si-SPAD detectors used for imaging purposes.

Structure of the thesis

The study consists of four chapters.

Chapter 1 contains a literature review composed of two main parts. Section 1.1 describes the importance of the 3D CMM in the automated process of manufacturing technologies for ensuring the quality of products. It is complicated to establish traceability of the 3D CMM because of versatility and complexity of

this measurement instrument. The entire traceability chain for the 3D CMM and traceability arrangement according to the international standards of the angle measurements for complicated geometrical objects are briefly described. The second part reviews the importance of Si-SPAD detectors used for assuring the accuracy of imaging in vision technologies. Full traceability according to the national primary standards is briefly covered to ensure an unbroken calibration chain.

Chapter 2 describes a method for dimensional measurements of complicated geometrical objects by the 3D CMM. Measurements were conducted for machined mechanical parts of a three-element optical photodetector. The measurement model and the results obtained are described in detail.

Chapter 3 presents the alignment position procedure developed, which was realized in a completely automated manner. Precise alignment position of the Si-SPAD detectors plays an important role in the investigation of homogeneity and determination of detection efficiency of the Si-SPAD detector. Further, the effect of the beam diameter on the detector homogeneity is analyzed and presented in terms of relative deviation. The measurement model and the measurement results are described in detail.

Chapter 4 focuses on the development of a high accuracy measurement method for the calibration of the detection efficiency of Si-SPAD detectors. Double filter transmission technique and integrating sphere were employed. The measurement model, the method, the setup, and research results are described in detail.

1. LITERATURE REVIEW

This chapter includes an overview of the current state-of-the-art in metrology used for Coordinate Measuring Machines (CMMs) and SPAD detectors applied for imaging in vision technologies.

1.1 Overview of 3D CMM Metrology

Manufacturing is the activity of producing components, products and systems, being one of the most important engineering activities. Economic success is linked directly to the development of user-driven, favored, manufacturing capabilities. It is important to record and collect data digitally during the development of the operation process. This knowledge, when properly used, makes it possible to save resources and time in the manufacturing of prototypes. Furthermore, the use of these data in digital manufacturing systems through Computer Aided Manufacturing (CAM) technology helps to maintain the quality of mass production, as can be seen in Figure 1.1 [8].

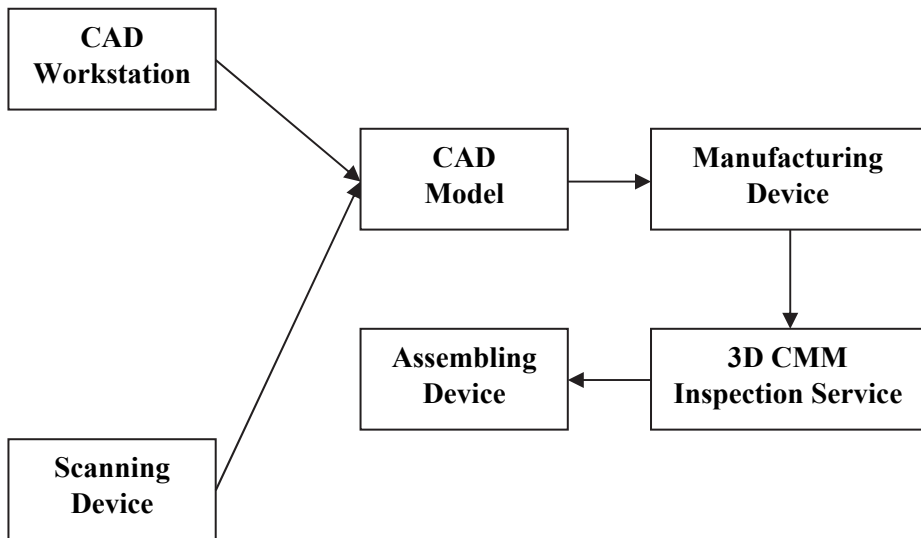


Figure 1.1 Flowchart of manufacturing product design using CAM [8]

CAM is the use of computer software for equipment control in all manufacturing activities, as shown in the flowchart of Figure 1.1 [8]. According to this flowchart of the automation process, it is clear that 3D Coordinate Measuring Machines (CMMs) play an important role in ensuring the quality of the product. 3D Coordinate Measuring Machines (CMMs) are universal measurement instruments in dimensional metrology. As one of the most powerful and versatile

metrological instruments, CMMs are widely used in most industrial applications, large and small in volumes [7]. Furthermore, 3D CMMs are intended for general purpose applications to achieve accurate dimensions of the measurement product where the operation probe system will identify the type of the measurement instrument usage like a contact or a non-contact probing system. Figure 1.2 shows the most common types of 3D CMM configurations according to [7].


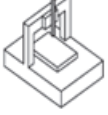
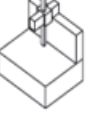
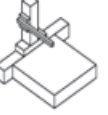
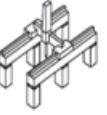
	Moving Bridge	Fixed Bridge	Cantilever	Horizontal Arm	Gantry
Applications/ Configuration					
General-purpose application	X	X	X	X	
Accuracy	X	X (gage Calibration)			
Large parts				X (large coatings, car bodies)	X (large vehicles, aerospace structures)

Figure 1.2 Summary of most common 3D CMM configurations associated with their general applications [7]

In principle, the function of the 3D CMM consists of the measurement of the regular or complicated shapes of the workpiece and in accordance with the series standard ISO 10360, the 3D CMM will evaluate the metrological information such as size, distance, form, angle, radius, orientation and location [7, 9-18]. An example of the modeling of workpiece geometry for 3D CMM metrology is illustrated in Figure 1.3.

The 3D CMM receives data points in terms of object coordinates measured at the surface of a certain of workpiece by using a guide to linearity transfer of the probing system along the X, Y and Z axes. In every 3D CMM, the software is installed to control coordinate transformation and to evaluate relevant geometric elements, such as size, distance, form, angle, radius, orientation, and location. Based on software operation, the required workpiece features are evaluated by combining the substitute elements and comparing dimensions and tolerances with the drawing given [7, 9-18].

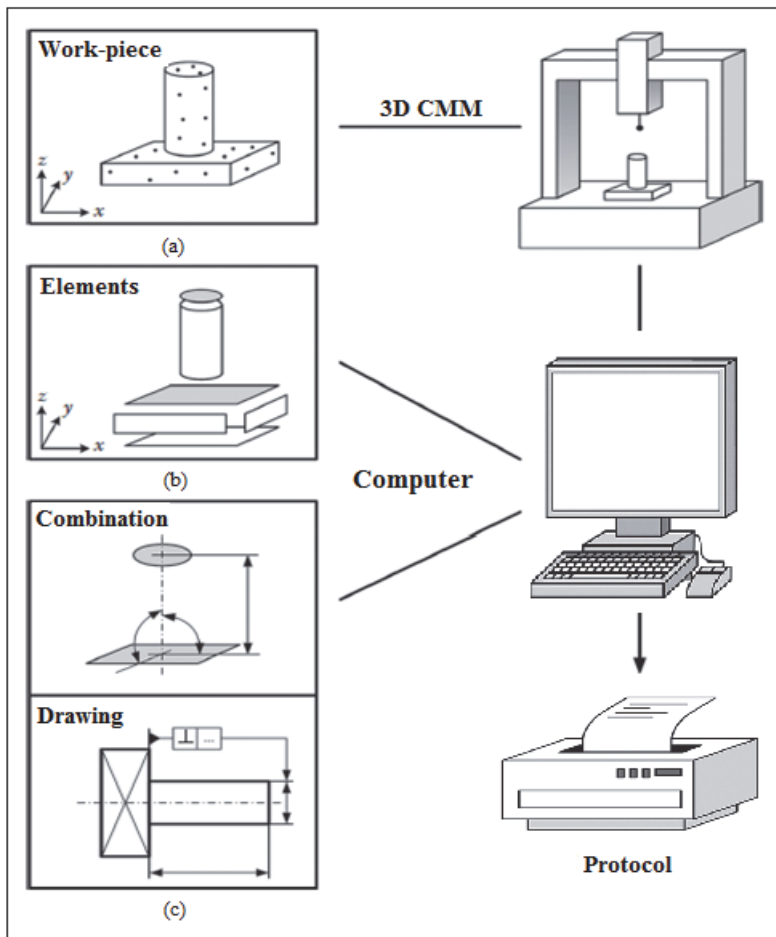


Figure 1.3 Illustration of the nature of CMM Metrology: (a) generating measurement data from CMM; (b) calculating the relevant substitute (mathematical) geometric elements in terms of parameters specifying size, distance, form, angle, radius, orientation and location; (c) evaluating the required workpiece features [7]

The entire traceability chain for 3D CMM is shown in Figure 1.4 [19].

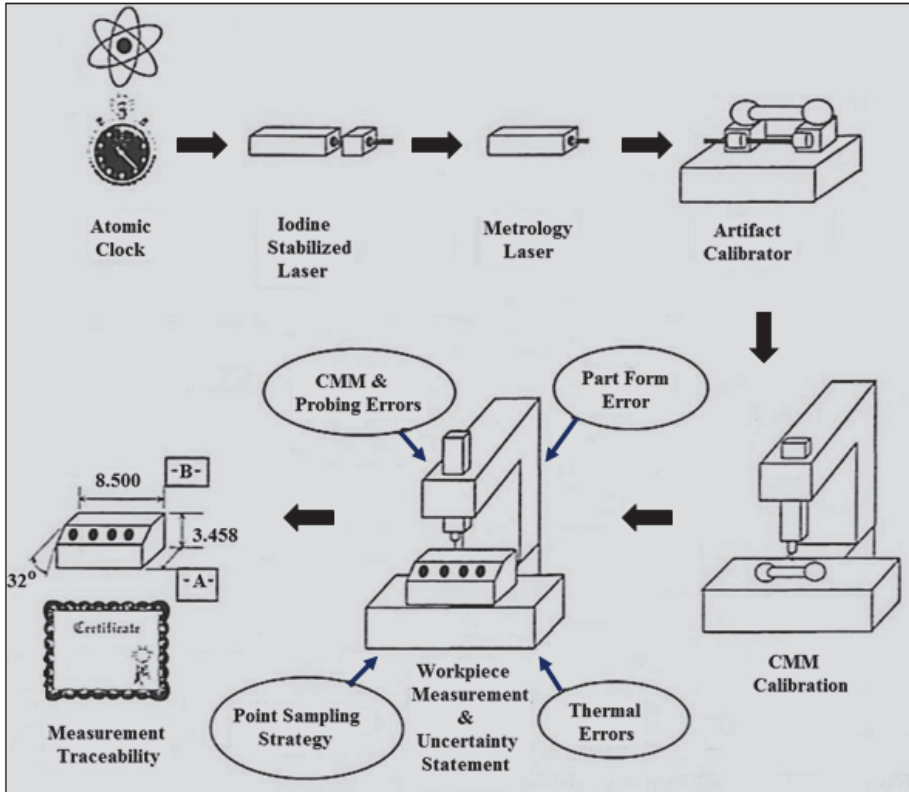


Figure 1.4 Traceability chain for CMM [19]

According to [19], traceability is established in a multi-step process, going all the way back in an unbroken sequence to national or international standards. The function of the 3D CMM, as a dimensional measurement instrument, entails a comparison of measured results to a standard of length [7]. The measurements by using the 3D CMM need to be traceable to the *meter*, which is one of the International System of Units (SI) [7, 20]. On the other hand, uncertainty of the length is determined by uncertainty in the measurements of intervals of time [7, 19]. Each step contributes an uncertainty, therefore in developing the final estimate, task-specific uncertainty and traceability statements must be distinguished [19]. The most complicated part in the establishment of traceability of the 3D CMM can result from versatility and complexity of this measurement instrument.

Chapter 2 will describe in detail the developed measurement model, the method and the standard uncertainty estimation of the measured angles for a complicated geometrical object, such as mechanical parts of a photodetector with a sophisticated construction.

1.2 SPAD detectors for imaging purposes

In many industrial and non-industrial applications, machine vision has been used to ensure automatic inspection and analyses through an imaging-based technology. The accuracy of imaging is a key parameter that influences the quality of many applications of vision technology. Nowadays, the Time of Flight (TOF) camera is revolutionizing the vision technology by ensuring high accuracy 3D imaging through using a complementary metal–oxide–semiconductor (CMOS) pixel array and a modulated light source [21-24]. Some of these important applications of the TOF technology are shown in Figure 1.5.

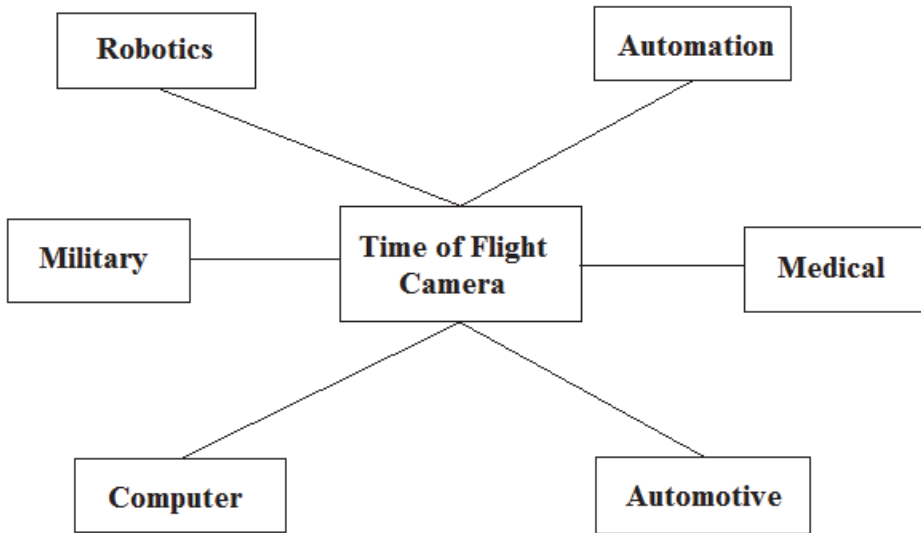


Figure 1.5 Schematic view of some important applications of TOF technologies [22, 25]

The basic principle of the TOF camera operation is illustrated in Figure 1.6. It is shown that the camera transmits modulated light (pulsed source) and measures its reflections on the scene [21]. From the reflected light, pulse modulation can be obtained by using a fast photodetector such as a single photon avalanche diode (SPAD) detector [22]. The perfect time resolution for detecting the photons at the arrival time enables SPAD detectors to yield high performance realization of 3D image sensors based on the TOF operations [25].

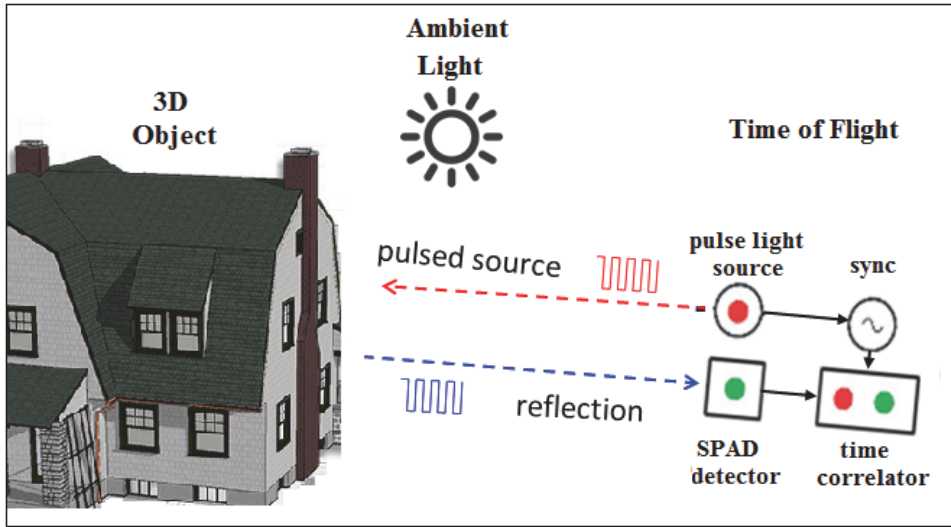


Figure 1.6 Illustration of the principle of TOF camera operation [21, 22, 26]

One of the most useful detectors in quantum operations for imaging purposes is the silicon single photon avalanche diode (Si-SPAD) detector where the detection efficiency plays an important role. A major advantage of the Si-SPAD detector lies in its integration capability with a standard CMOS fabrication. This is a promising technology for combining the SPAD with quenching circuits and time resolving circuits for time correlated single photon counting and TOF for producing a 3D image [27, 28]. SPAD detectors are very useful in the TOF techniques due to their picosecond time resolution. The pulses from a light source vary across different ranges of time resolution from 350 picoseconds up to 6.6 picoseconds. In today's conditions, to achieve 1 millimeter distance accuracy timing at room temperature, a pulse of 6.6 picoseconds is required, which is almost impossible with the present Silicon technology [22]. Thus, a multi-measurement technique, such as a time correlator, has been employed to achieve 6.6-picosecond time resolution, as can be seen in Figure 1.8. Additionally, there are different types of the CMOS fabrication; an example of the CMOS 8x8 SPAD Array is shown in Figure 1.7 [29].

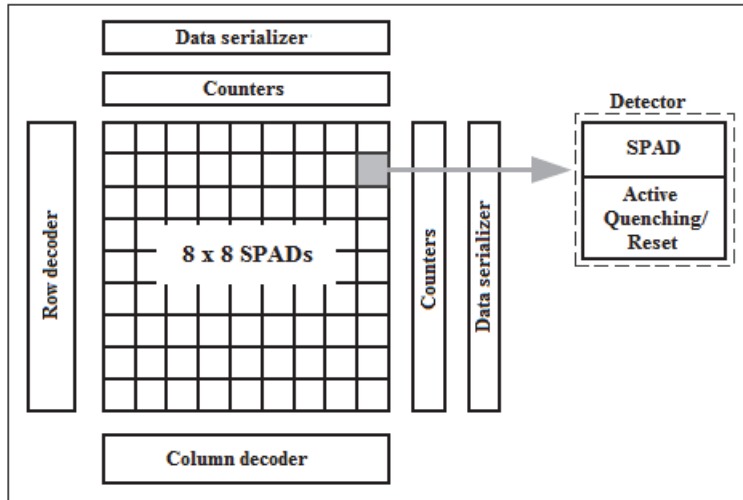


Figure 1.7 Block diagram of the CMOS 8x8 SPAD Array for the TOF operation [29]

Further, Chapters 3 and 4 will characterize the Si-SPAD detectors, the key component for improved accuracy of imaging in the vision technologies. According to Chapter 4, high accuracy methods have been developed for determination of quantum detection efficiency of the Si-SPAD detector and investigation of the quantum detection homogeneity of Si-SPAD detectors.

Full traceability to the national primary standards is assured via an unbroken calibration chain, as can be seen in Figure 1.8 [36]. According to [36], the detection efficiency is determined from the measurement of the photon count rate of the Si-SPAD and its comparison to the incoming photon flux, which is measured with a calibrated Si photodiode and calibrated attenuators (Filter transmission). Improvement of the detection efficiency of the Si-SPAD detector by using a new configuration setup is explained in detail in the following chapters.

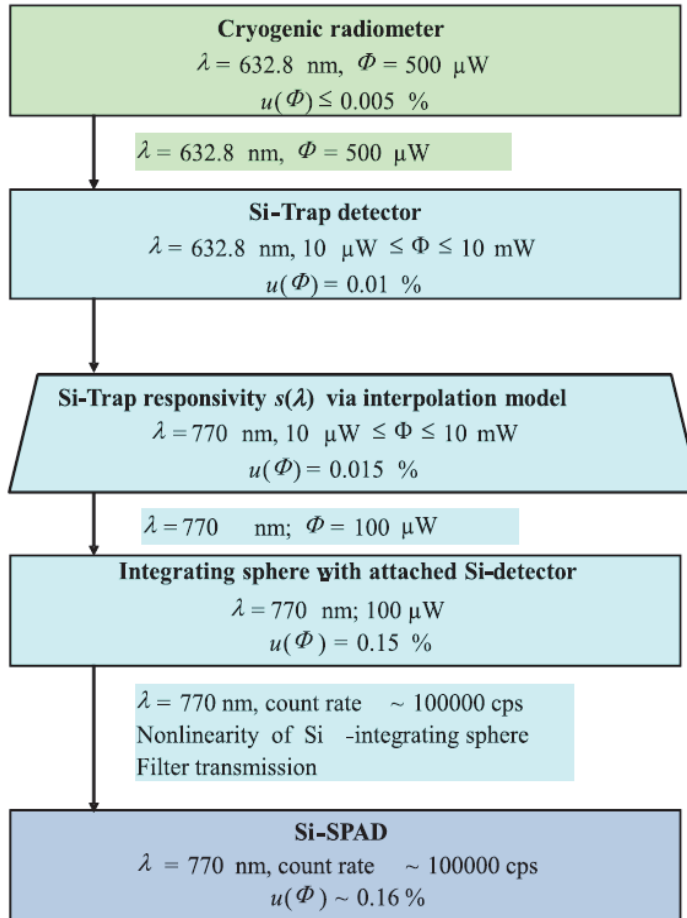


Figure 1.8 Calibration chain for the determination of the Si-SPAD detection efficiency at PTB, λ is wavelength and Φ is radiant power [36]

2. ANGLE MEASUREMENT METHOD FOR UNCERTAINTY EVALUATION OF COMPLICATED GEOMETRICAL OBJECTS BY USING THE COORDINATE MEASURING MACHINE

Many of the research works in relation with angle measurements have growing interest in certain industrial sector to respond their demands for increasingly strict tolerances tied to the production of mechanical pieces [33, 46-48]. The advantages by applying 3D CMM for determination of the angle measurements lies in degree of automation, obtaining data from pieces of different shapes and dimensions with maximum permissible error, reliability and accuracy [33, 49-55]. Different scientific research in 3D CMM have been focused in determination of angles of the regular geometrical objects which corresponds to 90° . The needs for determination the angle measurements in complicated geometrical objects by using 3D CMM has attracted major research interest. The current research has aimed to develop a novel method for angle measurement method for complicated geometrical objects by using 3D CMM.

2.1 Measurement instrument and methodology

Angle measurements of the three-element photodetector with a complicated geometrical form were conducted using a 3D Coordinate Measuring Machine manufactured by the Swiss Company called TESA factory. Owing to versatility and complexity measurement instrument, we have used a simplified case for traceability arrangement of the 3D CMM in relation to our research task for the determination of angle measurements of the complicated geometrical objects shown in Figure 2.1.

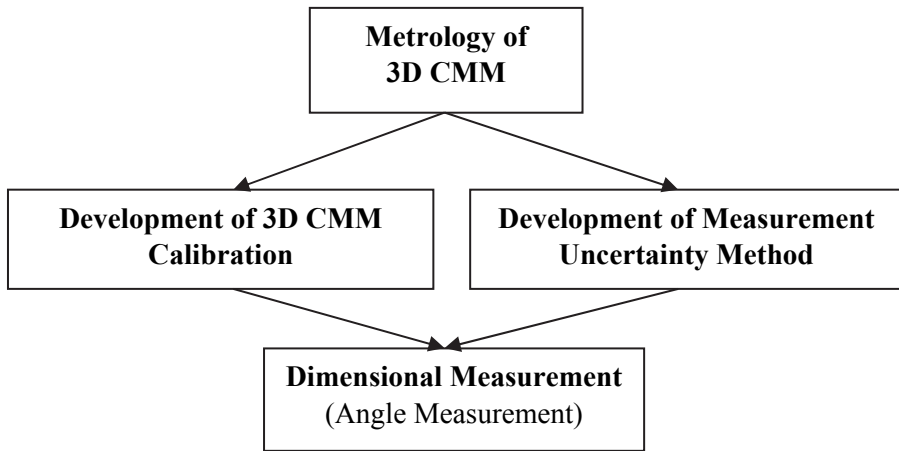


Figure 2.1 3D CMM traceability arrangement for the determination of angle measurements

Based on the traceability arrangement of angle measurements by using the 3D CMM and the series ISO 10360 standard, we have developed contributor factors of the 3D CMM that need to be considered during the calibration process, as shown in Figure 2.2.

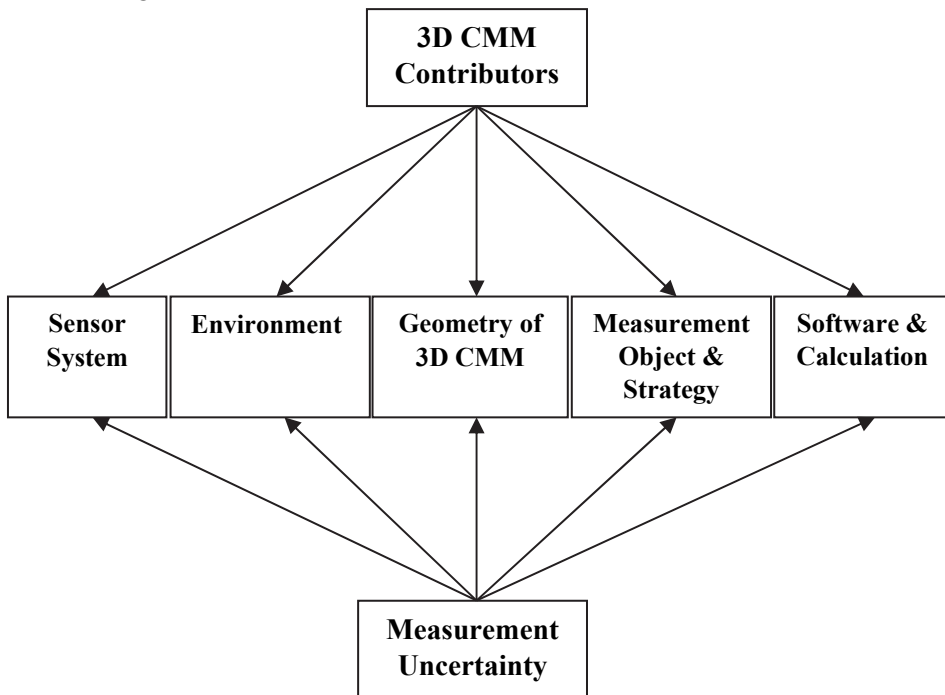


Figure 2.2 Flowchart of 3D CMM contributors

The TESA MICRO-HITE 3D coordinate measuring system is an affordable high accuracy measuring instrument designed to fill the operational gap between precision hand-held measuring instruments and high-end coordinate measuring machines [30]. The layout of the TESA MICRO-HITE 3D CMM used for the measurement setup is shown in Figure 2.3.



Figure 2.3 Layout of the measurement setup: 1 – moving bridge; 2 – guide in 3D (X/Y/Z); 3 – exchangeable probe accompanied with probe command button; 4 – calibration ball; 5 – workpiece place; 6 – measuring range volume; 7 – software controller

The measurement principle of this 3D CMM consists of the contacting surface of a measurement object with a touch probe to the surface of the measurement object. A guide to linearity transfers the probing system along the X/Y/Z axes and can run at determined angles to each other. Furthermore, the TESA REFLEX program controller recognizes the dimensional measurements that arise from contacting the touch probe at the surfaces. Interactive software will allow complex measurements in a precise and routine way. The measuring range volume (X/Y/Z) of the TESA MICRO-HITE 3D CMM is equal to 460 mm x 510 mm x 420 mm with the resolution $R = 0,1 \mu\text{m}$, as stated by the manufacturer.

A complicated geometrical shape, such as a three-element photodetector body with an approximate volume size 40 mm x 32 mm x 32 mm, has been used to determine the dimensional accuracy (incidence angle) of this photodetector. The

photodiode type used is S1337-11 (windowless) from Hamamatsu. It is important to mention that photodiodes should be mounted in the three-element body part under radiation incidence angle close to 45° where for the best performance, the declination angle between the incoming and the outgoing beams for the photodiode should be less than $\pm 0,2^\circ$. This angle declination affects the reflection from the photodiode active surface and, thus, transmittance and responsivity of the whole detector [31].

The measurement method is characterized by two measurement strategies to determine the incidence angle in the three-element photodetector. Firstly, the standard measurement procedure offered by the 3D CMM to guarantee the performance of the 3D CMM according to the manufacturer specification is applied and, secondly, the novel measurement procedure has been developed in relation to the specific needs, such as the determination of the incidence angle of the three-element photodetector. The measurement procedure for the determination of the incidence angle of the three-element photodetector illustrated in Figure 2.4 is outlined below in the following text.

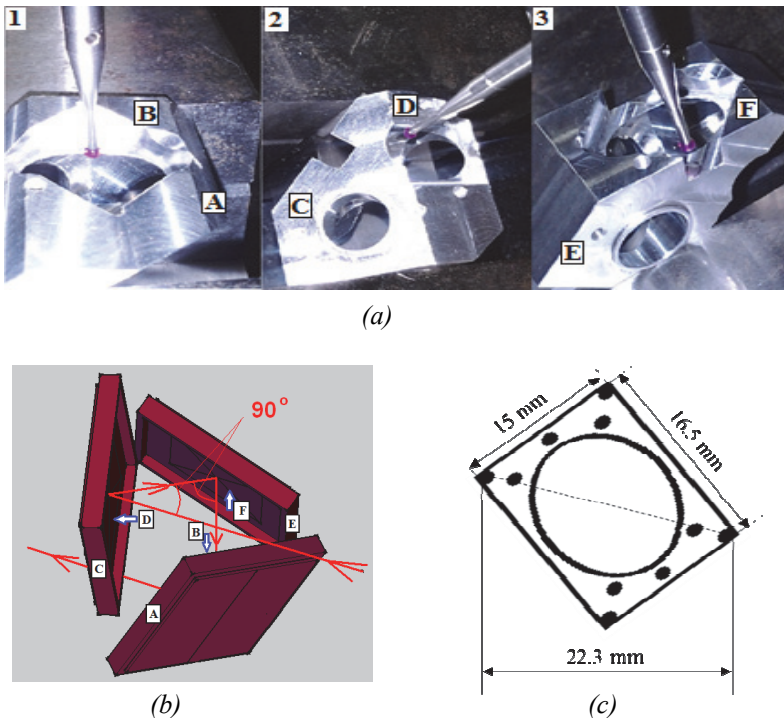


Figure 2.4 Illustration of the determination of the angle of photodetector: (a) Top view illustration picture of the angle determination of photodetector, (b) - scheme of three photodiodes aligned in the photodetector, the beam indicating the optical path between the centers of photodiodes shown as an arrowed line; (c) - schematic view of the photodiode active plane associated with uniform distributed measurement points (filled dots)

The measurement procedure starts with the calibration of the touching probe at the calibration ball of the 3D CMM shown in the layout picture of Figure 2.3. The touching probe was mounted in vertical positions under 0° angle and the calibration was realized on the distributed points around the calibration ball. Based on the instruction in the manual of the machine, to have accurate positions of the touching probe, the criteria of the distributed points were used, which should not be less than six points. Following a successful calibration position, the three-element photodetector body part is placed in the workpiece to continue the measurement procedure, as shown in Figure 2.4. In the measurements, angles were determined between the pairs of planes AB (position 1), CD (position 2) and EF (position 3). The measurements were conducted in the reference planes A, C, E and across the active planes B, D, F to cover each entire plane of the photodiode as uniformly as possible, as can be seen in Figure 2.2 a,b. The planes A, D, E were chosen as the reference planes because of their connection design with the planes of the active areas B, D and F. The planes B, D, and F were assumed to be parallel with the planes of photodiode active surfaces, i.e. close to 45° in relation to reference planes. The uniform distribution readings for each active plane of the three photodiodes are shown in Figure 2.2 c. The maximum distance between the measurement points for each active plane was 22,3 mm. The maximum distance was used to determine some uncertainty components that arise from calibration and the measuring distance between two points of the 3D CMM. The number of the readings taken during the measurements for each angle plane was ten.

2.2 Measurement model

In accordance with [32], the measurement model can be expressed as follows:

$$y = x + \sum_{i=1}^n \delta x_i , \quad (2.1)$$

where y – estimate of the output quantity,
 x – measured value,
 δx_i – corrections that arise from input quantities.

There is large number of uncertainty sources due to versatility and complexity of the 3D CMM, which makes the evaluation of the measurement uncertainty a multifaceted problem. In the following, it will be shown that some sources of uncertainty mentioned in Chapter 1 can influence in the measurement results. Thus, the measurement model can be expressed by the following equation:

$$y = x + \delta x_{\text{cal}} + \delta x_{\text{probe}} + \delta x_{\text{read}} + \delta x_{\text{rep}} + \delta x_L , \quad (2.2)$$

where δx_{cal} – correction from the calibration of the machine,
 δx_{probe} – correction from the probing error,
 δx_{read} – correction from the reading of indication,
 δx_{rep} – correction from repeatability,
 δx_L – correction from the distance between two points.

2.3 Evaluation of measurement uncertainty and research results

Evaluation of the measurement uncertainty of the angle of a three-element photodetector by using the 3D CMM has been determined according to the Guide to the expression of uncertainty in measurement (GUM) [32]. In general cases, output quantity y is not measured directly but rather is estimated from the input quantities mentioned in the above measurement model (Eq. (2.2)). Furthermore, all input quantities x in the measurement model during the estimation process can be characterized with a combined standard uncertainty.

The combined standard uncertainty of uncorrelated input quantities is determined by the following equation:

$$u_c(y) = [c_i^2 \cdot u(\delta x_i)^2]^{1/2} = [c_1^2 \cdot u^2(\delta x_{\text{cal}}) + c_2^2 \cdot u^2(\delta x_{\text{prob}}) + c_3^2 \cdot u^2(\delta x_{\text{read}}) + c_4^2 \cdot u^2(\delta x_{\text{rep}}) + c_5^2 \cdot u^2(\delta x_L)]^{1/2}, \quad (2.3)$$

where c_i – sensitivity coefficients for all input quantities,
 $u(\delta x_i)$ – standard uncertainty of the input quantities.

The standard uncertainties of all input quantities were determined under the following circumstances.

In the measurement process, the calibration of the TESA MICRO-HITE 3D CMM was not realized due to the manufacturing specifications certificate of this device, which is based on the availability usage of the measuring time period. Therefore, in relation to our particular case for the determination of the accuracy of the 3D CMM, we have not considered the whole volume of the machine but only the volume of the three-element photodetector body which was subjected to the measurements. According to [30], uncertainty from the calibration of the 3D CMM in X, Y and Z axis can be expressed by the following equation:

$$u(\delta x_{\text{cal}}) = \frac{0,003 + \frac{4 \cdot L}{1000}}{k}, \quad (2.4)$$

where k – coverage factor, in our case $k = 2$ for the level of confidence of approximately 95 %,

L – distance between two points.

The distance L can be referred to the maximum distance between the two measurements points of the pairs of planes. According to [33], the distance between the two points is calculated as follows:

$$L = [(x_2 - x_1)^2 + (y_2 - y_1)^2 + (z_2 - z_1)^2]^{1/2} \quad (2.5)$$

Estimation of the uncertainty of the probing error can be related to the form error of the touching probe used before starting the measurement procedure. The calibration of the touching probe was realized by contacting the probe six times around the calibration ball mounted in the measurement table of the 3D CMM, as can be seen in Figure 2.1. TESA REFLEX software controller recognizes the measurements that come from the calibration ball. The diameter of the calibrated touching probe was 2 mm and uncertainty of the form error can be expressed as follows:

$$u(\delta x_{\text{prob}}) = [u^2(\delta x_{\text{F.Error}})]^{1/2} \quad (2.6)$$

Standard uncertainty due to the readings of the angle measurements between the pairs of the planes was determined by the standard deviations of the readings, as expressed in the following equation:

$$u(\delta x_{\text{read}}) = S(\delta x_{\text{read}}) = \left[\frac{1}{n-1} \sum_{i=1}^n (x_i - x_m)^2 \right]^{1/2}, \quad (2.7)$$

where n – number of independent observations,
 x_i – observed readings,
 x_m – mean value of the readings.

Standard uncertainty due to repeatability was determined from the two series of the standard uncertainty of the readings in accordance with the following equation:

$$u(\delta x_{\text{rep}}) = \left[\frac{u^2(\delta x_{\text{read1}}) + u^2(\delta x_{\text{read2}})}{2} \right]^{1/2} \quad (2.8)$$

Evaluation of the standard uncertainty due to the distance between the two points was determined through the statistical behavior model of the 3D CMM. Using this model, the errors of the machine used related to orientation and length in the working volume were investigated. According to [33], uncertainty from the distance between the two points can be expressed as follows:

$$u(\delta x_L) = \left[L^2 \frac{E_k^2}{3} + \frac{E_G^2}{3} + \frac{R^2}{3} \right]^{1/2}, \quad (2.9)$$

where R – resolution of the 3D CMM,
 E_k – parameter due to the specification of the 3D CMM, which can be related to the maximum permissible measuring error of the linear spatial diagonal of the measuring volume,
 E_G – parameter due to the specification of the 3D CMM which can be related to the maximum permissible probing error.

The sensitivity coefficients (Eqs. (2.13) – (2.15)) were evaluated through the partial derivatives of the equations expressed as follows [33]:

$$\cos\alpha = \frac{x_2 - x_1}{[(x_2 - x_1)^2 + (y_2 - y_1)^2 + (z_2 - z_1)^2]^{1/2}}, \quad (2.10)$$

$$\cos\beta = \frac{y_2 - y_1}{[(x_2 - x_1)^2 + (y_2 - y_1)^2 + (z_2 - z_1)^2]^{1/2}}, \quad (2.11)$$

$$\cos\gamma = \frac{z_2 - z_1}{[(x_2 - x_1)^2 + (y_2 - y_1)^2 + (z_2 - z_1)^2]^{1/2}} \quad (2.12)$$

These partial derivatives describe how the output estimate y varies with changes in the values of the input estimates x_i [32]. In our particular case, we have $\cos\alpha = \cos\beta = \cos\gamma$ and $x_{21} = x_2 - x_1$, $y_{21} = y_2 - y_1$, $z_{21} = z_2 - z_1$. The maximum of the partial derivatives was chosen from $\frac{\partial \cos\alpha}{\partial x}$; $\frac{\partial \cos\alpha}{\partial y}$; $\frac{\partial \cos\alpha}{\partial z}$ and determined by the following equations:

$$c_1 = \frac{\partial \cos\alpha}{\partial x} = \frac{(x_{21}^2 + y_{21}^2 + z_{21}^2)^{1/2} - x_{21} \frac{2x_{21}}{2(x_{21}^2 + y_{21}^2 + z_{21}^2)^{1/2}}}{x_{21}^2 + x_{21}^2 + z_{21}^2} = \frac{x_{21}^2 + y_{21}^2 + z_{21}^2 - x_{21}^2}{(x_{21}^2 + y_{21}^2 + z_{21}^2)^{3/2}} = \frac{y_{21}^2 + z_{21}^2}{(x_{21}^2 + y_{21}^2 + z_{21}^2)^{3/2}}, \quad (2.13)$$

$$c_2 = \frac{\partial \cos \alpha}{\partial y} = \frac{-x_{21} \frac{2y_{21}}{2(x_{21}^2 + y_{21}^2 + z_{21}^2)^{1/2}}}{x_{21}^2 + y_{21}^2 + z_{21}^2} = \frac{-x_{21} \cdot y_{21}}{(x_{21}^2 + y_{21}^2 + z_{21}^2)^{3/2}}, \quad (2.14)$$

$$c_3 = \frac{\partial \cos \alpha}{\partial z} = \frac{-x_{21} \frac{2z_{21}}{2(x_{21}^2 + y_{21}^2 + z_{21}^2)^{1/2}}}{x_{21}^2 + y_{21}^2 + z_{21}^2} = \frac{-x_{21} \cdot z_{21}}{(x_{21}^2 + y_{21}^2 + z_{21}^2)^{3/2}} \quad (2.15)$$

Hence, all standard uncertainties mentioned above associated with sensitivity coefficients were determined to evaluate the combined standard uncertainty. Afterwards, expanded uncertainty U was obtained through multiplication of the combined standard uncertainty $u_c(y)$ with a coverage factor, $k = 2$, as can be expressed in the following equation:

$$U = k \cdot u_c(y) \quad (2.16)$$

In the 3D CMM, due to the variety of the uncertainty contribution, uncertainty at the 95% confidence level was used at the coverage factor 2.

The results of the determination of each angle of the optical three-element photodetector body part associated with their uncertainty by using the 3D CMM are illustrated in Figure 2.5 and summarized in Tables 2.1 and 2.2.

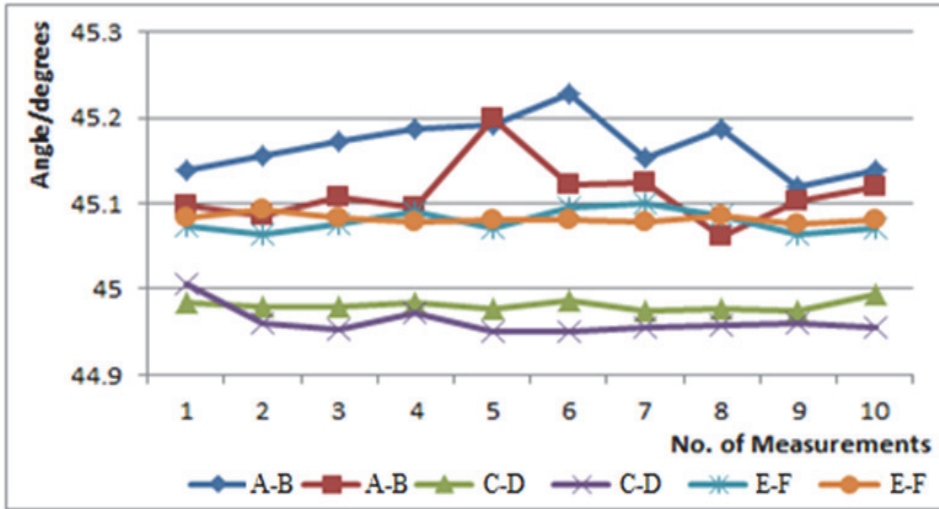


Figure 2.5 Repeatability of angle measurement results between reference planes A, D, E and across active planes B, D, F

Table 2.1 Uncertainty budget of angle measurements of the photodetector body part

Sources of Uncertainty	Standard Uncertainty	Probability Distribution	Sensitivity Coefficient	Uncertainty [°]
Calibration	$7,9 \cdot 10^{-2}$ [mm]	normal	$1,7 \cdot 10^{-2}$ [°/mm]	$1,4 \cdot 10^{-3}$
Probing error	$2 \cdot 10^{-3}$ [mm]	normal	$1,7 \cdot 10^{-2}$ [°/mm]	$3,4 \cdot 10^{-5}$
Readings	$3,5 \cdot 10^{-2}$ [°]	normal	1,0	$3,5 \cdot 10^{-2}$
Repeatability	$4,8 \cdot 10^{-2}$ [°]	normal	1,0	$4,8 \cdot 10^{-2}$
Distance	$7,8 \cdot 10^{-2}$ [mm]	rectangular	$1,7 \cdot 10^{-2}$ [°/mm]	$1,3 \cdot 10^{-3}$
Combined standard uncertainty, $k = 1$				$5,9 \cdot 10^{-2}$
Expanded uncertainty, $k = 2$				$1,2 \cdot 10^{-1}$

Table 2.2 Measurement results for the estimation of each angle measurement associated with expanded uncertainty

Angle	Estimated value [°]	Expanded uncertainty [°]
∠AB	45,11	0,12
∠CD	44,96	0,12
∠EF	45,08	0,12

The measurement results above fulfill the target mentioned in Section 2.1 ($45^\circ \pm 0,2^\circ$) for the determination of the angle of the three-element photodetector. The results show that an expanded uncertainty of the declination angle between the incoming and outgoing beams is $\pm 0,12^\circ$. This means that a three-element photodetector meets the specification of the mechanical manufactured part that will be used for a well-functioning detector in photonics.

The results of this study were implemented in the design of twelve element transmission trap detector to provide attenuation of a laser beam at the level of 1,5 parts per million for studies of single photon sources and detectors in European Metrology Research Programme (EMRP) at project Single-photon sources for quantum technologies (SIQUTE).

In the future, it will be necessary to improve larger uncertainty components that arise from the readings of indication and repeatability of the measurement results, which simultaneously will improve the overall measurement uncertainty of the angle measurement of the three-element photodetector.

3. ALIGNMENT POSITION METHOD FOR Si-SPAD DETECTOR CALIBRATION PROCESS AND INVESTIGATION OF THE DETECTION EFFICIENCY HOMOGENEITY

Silicon single-photon avalanche diodes (Si-SPADs) are the most common choice for single-photon detection in the visible to near-infrared spectral range up to 1000 nm [34, 35]. Si-SPADs play an important role in a variety of research fields, such as experimental quantum optics, quantum cryptography and quantum computing but also in medicine, biology, telecommunication and astrophysics applications [36]. The detection efficiency of a detector is one of the key parameters. However, most of the customers have to rely on the detection efficiency values given by the manufacturers or they have to measure the values themselves. Thus, in order to achieve reliable measurements, a compact setup for Si-SPAD calibration that uses traceable transfer standards has been recently established by PTB Germany [36, 37].

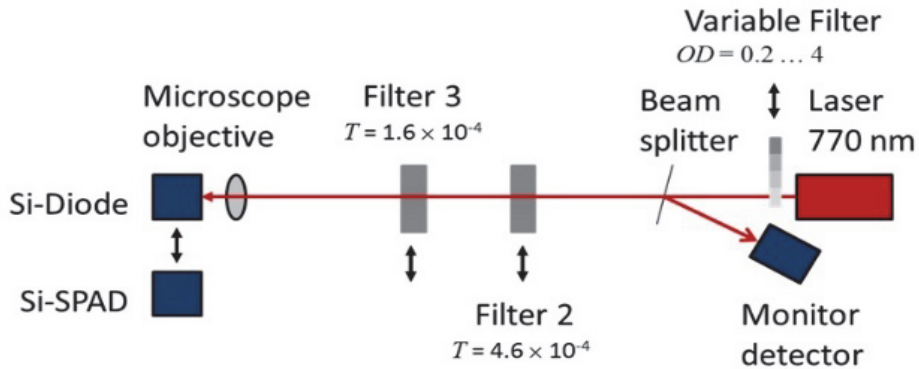
The previous research work [36] has stated the problem for optimization of the Si-SPAD detector position and investigation of the homogeneity. Alignment position were in manual way and before starting calibration process it takes almost 3 days. The alignment position of the Si-SPAD detector in the incident beam has to be established with high accuracy to achieve low uncertainty measurements. Also, it has to be assured that the laser beam used for the calibration is completely within the active area of the Si-SPAD and hits reproducibly the same location on the detector's active area. This requires some efforts and is very time consuming if aligned manually. The current research will be focused in accurate and automatic alignment of the Si-SPAD which will reduce the measurement time in 10 minutes and secondly will analyze the detection efficiency homogeneity for two commercial Si-SPAD detectors with different sensor diameters.

3.1 Measurement setup and method

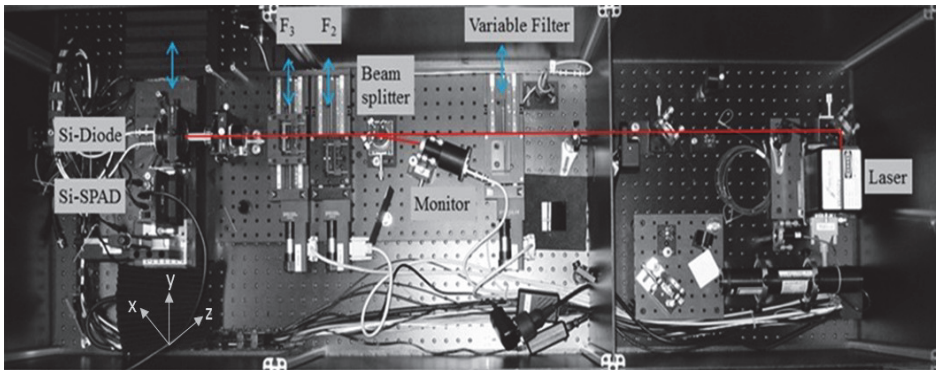
In the calibration process, alignment of the Si-SPAD detector with respect to the absolute position and to the reproducibility to re-align is of prime importance. The measurements of the detection efficiency of the Si-SPAD detector by using the double filter transmission technique will be explained in Chapter 4 by using a new configuration setup. Figure 3.1 shows the experimental setup used for the alignment of the Si-SPAD detector, which is based on the previous method for determination of the detection efficiency established at PTB [36, 37].

The setup in Figure 3.1 shows that the laser emits optical radiation on 770 nm wavelength with instability of less than 1 %, focused on a 20X microscope objective lens (Mitutoyo M Plan Apo, numerical aperture = 0,42, working

distance = 20 mm) on the detectors. A variable filter is used to adjust optical power in the laser beam. A beam splitter is used to split the beam of light in two where one transmits the light to the detector and the other reflects the light to the monitor detector. The monitor detector is used to reduce the instability of the laser optical power. Individual Filters 2 and 3 is moved in the beam path to measure the optical power with the standard Si-Diode and both Filters combined as well as the Si-SPAD have been moved in the beam path to measure the corresponding optical power with the Si-SPAD detector.



(a)



(b)

Figure 3.1 Setup for Si-SPAD detector calibration at PTB: (a) Schematic setup for determination of the detection efficiency of Si-SPADs; (b) top view of the setup for Si-SPAD detector calibration [36, 37]

The present measurement method will be focused on the alignment of the Si-SPAD detector by determining an absolute position for setting the detector prior to starting the calibration process of the Si-SPAD detector. The Si-SPAD detector with respect to the focused beam is aligned using motorized XYZ-translation stages in an automatic manner. The measurement procedure consists

in scanning the beam profile by using the Si-SPAD detector itself. The scanning is carried out before and after the focal plane, i.e. the working distance of the objective lens, as can be seen in Figure 3.2:

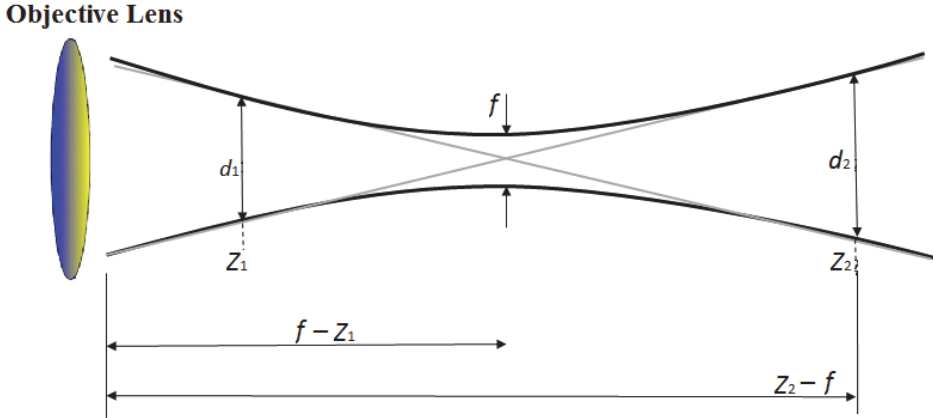


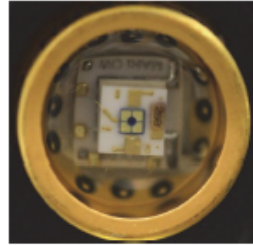
Figure 3.2 Schematic view for the determination of the objective focal plane accompanied with two measurement Gaussian beam profiles: f is the objective focal plane, d_1 and d_2 are beam diameters, Z_1 and Z_2 are beam distances

To find a criterion for the optimization of the Si-SPAD detector position with respect to the incoming laser beam, PTB is using the “Agilent VEE” programme for performing the automated measurement scan. The data is collected by scanning the detector with laser beam (in the X, Y plane) several times at various work distances Z from the microscope objective. For this measurement the environment setup was set with a work point reference position ($Z = 20$ mm) between the Si-SPAD detector window and the objective lens before starting the scan. The reference position is valid only for this measurement setup. In the three measurements, firstly, the two Gaussian beam profiles, which correspond to the front of and behind the objective focal plane and in the end, the objective focal plane (Rectangular profile), were determined. The scanning procedure was realized such that the Z -position of the detector was moved by 1 mm steps towards the microscope objective and for each Z position, a full (X, Y)-scan was performed. Two different types of Si-SPAD detectors with different sensor diameters ($\phi_{D1}=180$ μm and $\phi_{D2}=50$ μm) were used in the measurements, as can be seen in Figure 3.3. The (X, Y) scanning ranges for the SPCM-AQR-16 detector were 0,5 mm x 0,7 mm and for the MPD detector, 0,2 mm x 0,4 mm with a resolution of 0,01 mm. This scanning procedure allowed us to find the optimum (X, Y, Z)-position of the Si-SPAD detector with respect to the incoming beam.

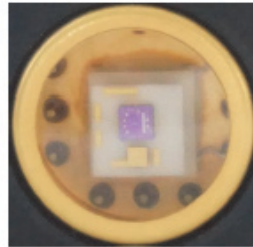
Single Photon Counting Module



Sensor



(a)



(b)

Figure 3.3 Si-SPAD detectors used in measurements: (a, b) Single Photon Counting Modules (left) and their corresponding sensors (right); (a) SPCM-AQR-16(PerkinElmer) and (b) PDM (Micro Photon Devices) [38, 39]

Figure 3.3 shows the pictures of Si-SPAD detectors used in the measurements; the characteristics of these detectors are as follows:

- The first type SPCM-AQR-16 (Perkin-Elmer) is a self-contained module with a circular active area. The detection efficiency exceeds 70% at 650 nm for 180 μm detector diameter where the dark counts are 250 counts/s [38].
- The second type is a PDM series photon counting detector module with a square active area whose peak photon detection efficiency over a 50 μm diameter detector exceeds 49% at 550 nm and dark counts 49 counts/s [39].

3.2 Si-SPAD detector alignment

The accurate method for determining the optimal position of the Si-SPAD detector and the investigation of the homogeneity are based on the evaluation of these important steps:

- centroid and the diameter of each measured beam profile,
- objective focal plane,
- Gaussian fitting curve,
- error from Gaussian fitting curve,
- relative standard deviation within the selected region.

The MATLAB program was implemented to the Agilent VEE program to evaluate the steps mentioned above automatically.

Firstly, the centroid and the diameter of each measured beam profile were determined by the following equations:

$$x_{\text{center}} = \frac{\sum_{i=1}^N x_i \cdot s_i}{\sum_{i=1}^N s_i}, \quad (3.1)$$

$$x_{\text{diameter}} = x_{i,\text{max}} - x_{i,\text{min}}, \quad (3.2)$$

$$y_{\text{center}} = \frac{\sum_{i=1}^N y_i \cdot s_i}{\sum_{i=1}^N s_i}, \quad (3.3)$$

$$y_{\text{diameter}} = y_{i,\text{max}} - y_{i,\text{min}}, \quad (3.4)$$

where s_i – modified irradiance distribution over a scanning region
 $(S_{x_i, y_i} \geq \text{threshold})$,
 x_i, y_i – scanning position in (X, Y)-coordinate directions.

The objective focal plane that approximated the beam propagation to a simple geometric beam propagation (dashed line, Figure 3.3) was evaluated by the following equation:

$$f = \frac{d_1 \cdot Z_2 + d_2 \cdot Z_1}{d_1 + d_2}, \quad (3.5)$$

where f – objective focal plane,
 Z_1, Z_2 – beam distances,
 d_1, d_2 – beam diameters.

The calculation of the Gaussian fitting curve is based on the function of the form, as can be seen in the following equation:

$$f(Y) = a \cdot \exp\left(\frac{(Y - b)^2}{2 \cdot \sigma^2}\right), \quad (3.6)$$

where a – height of the curve's peak,
 b – center position of the peak,
 σ – standard deviation of the count rate,
 Y – scanning positions in the y-direction.

The error from the Gaussian fitting curves was evaluated by the following equation:

$$\text{Error (\%)} = \text{Gaussian (Model)} - \text{Gaussian (Measurement)} \quad (3.7)$$

The minimum error from the Gaussian fitting curve will give information for two scan beam profiles that can be performed in front of and behind the objective focal plane.

The relative homogeneity was obtained for the mean quantum detection within the selected region (regions 1 and 2 in Figure 3.6) and evaluated through the relative standard deviation (RSD) by the following equation:

$$RSD = \frac{100 \cdot \sigma}{x_m}, \quad (3.8)$$

where σ – standard deviation of the count rate within the selected region,
 x_m – mean value of the count rate within the selected region.

3.3 Research Results

3.3.1 Results of Si-SPAD alignment position

The measurement results for three performed scans of the SPCM-AQR-16 detector in relation to the different Z – positions are summarized in Table 3.1 and illustrated in Figures 3.4 – 3.6. For the Z – position 13,6 mm (closer to objective lens), the scan profile corresponds dominantly to the Gaussian beam profile where the error from the Gaussian fitting curve is equal to 8,1 %. The other dominantly Gaussian profile corresponds to the Z – position 15,6 mm, which is 2 mm away from the reference position and the error from the Gaussian fitting curve is closer to 8,5 %. For the Z – position 14,6 mm, calculated from the

objective focal plan, the scan profile corresponds dominantly to a rectangular profile.

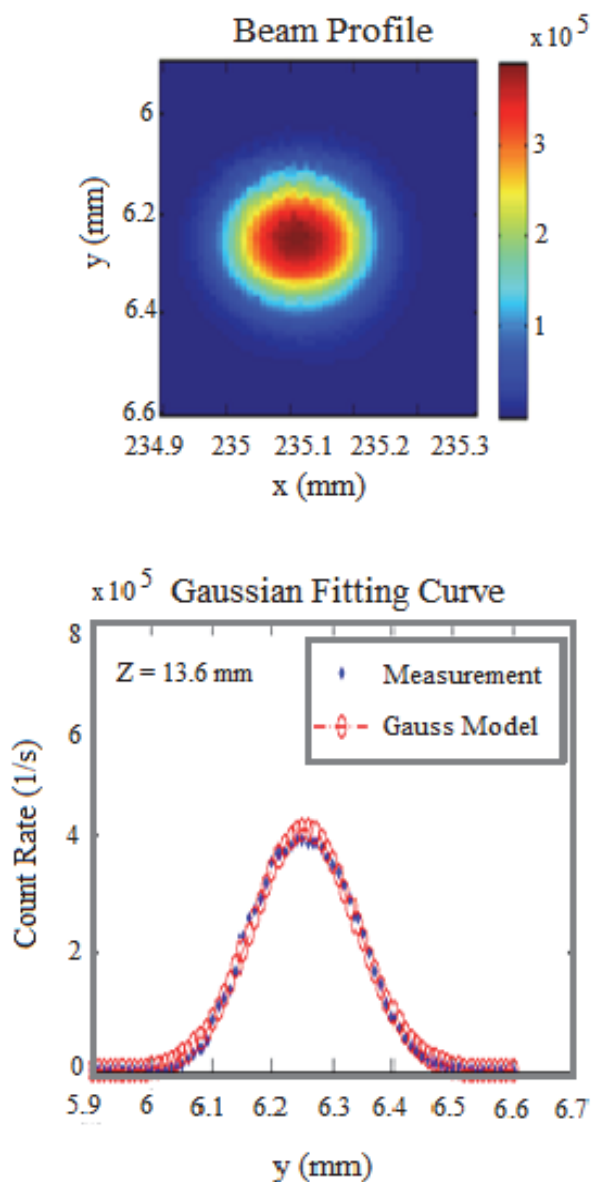


Figure 3.4 Scanning results for the SPCM-AQR-16 detector at position $Z = 13,6$ mm

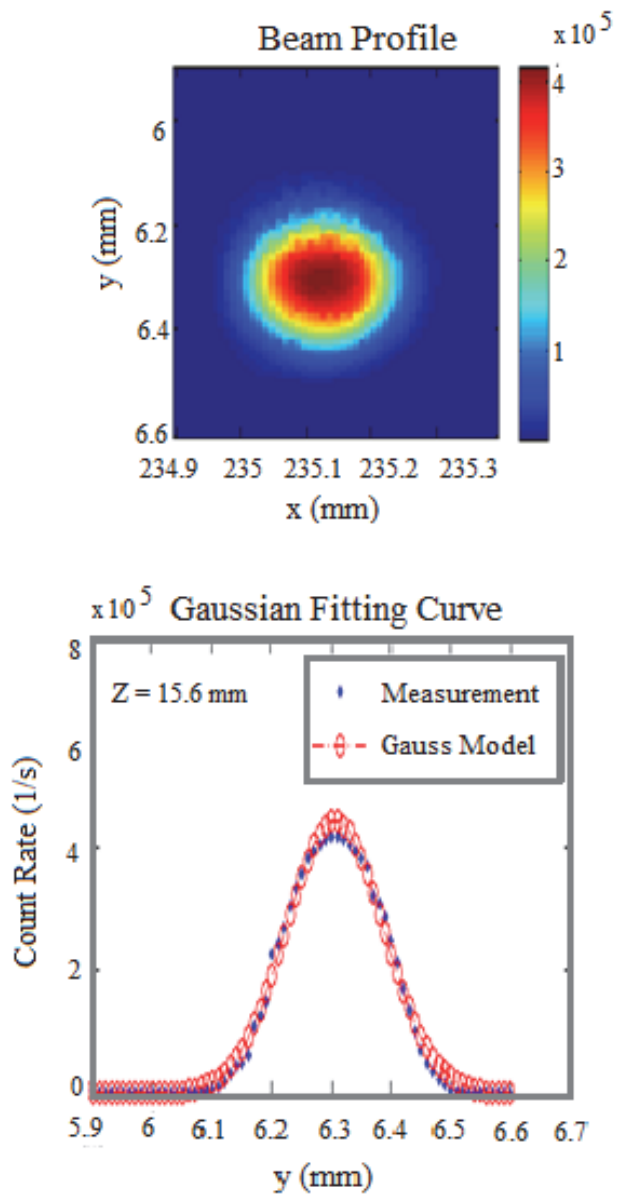


Figure 3.5 Scanning results for the SPCM-AQR-16 detector at position $Z = 15,6$ mm

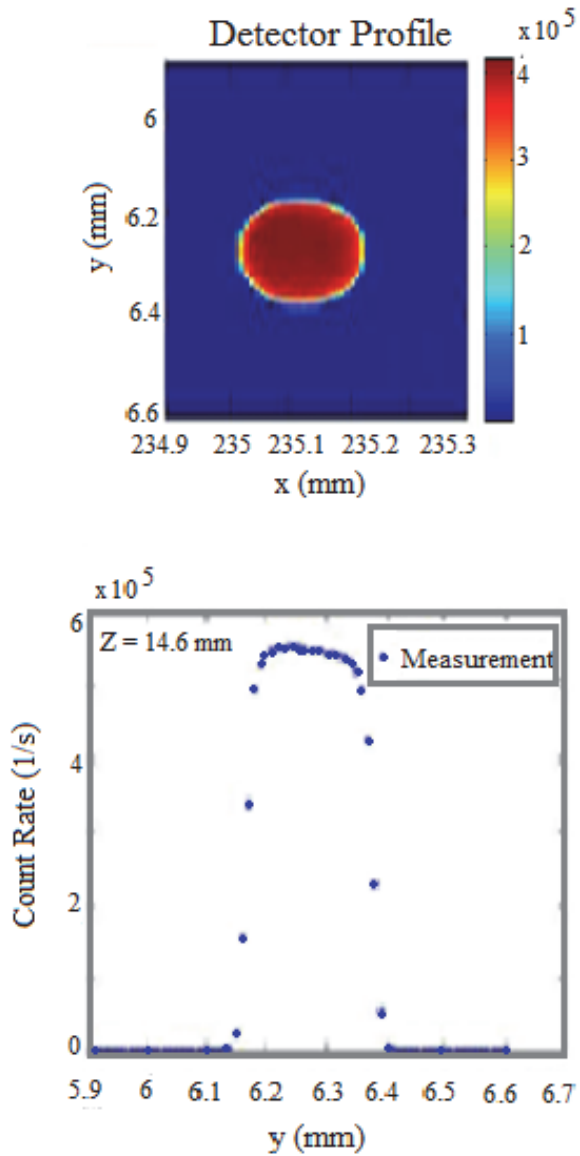


Figure 3.6: Scanning results for the SPCM-AQR-16 detector at position $Z = 14,6$ mm

Table 3.1 Summary results of the SPCM-AQR-16 detector

No	Z – position (mm)	x – center (mm)	y – center (mm)	Error (%)	Diameter (mm)
1	13,6	235,11	6,26	8,1	0,35
2	14,6	235,11	6,28	-	0,22
3	15,6	235,12	6,30	8,5	0,35

According to Eq. (3.7), the error calculated from the Gaussian fitting curve was used to obtain distinct information of the presence of the Gaussian profile. Minimizing the error will give information for the position and diameter of the measured beam profile. On the basis of this information and the scanning results, we have determined the optimal (X, Y, Z) - position for the detector. It is in the (X, Y) - center position of the scan profile with the smallest diameter, i.e. at $x_{\text{center}} = 235,11 \text{ mm}$, $y_{\text{center}} = 6,28 \text{ mm}$ and $Z = 14,6 \text{ mm}$.

The results of the three PDM detector scans in relation to the different Z - positions are summarized in Table 3.2 and Figures 3.7 – 3.9.

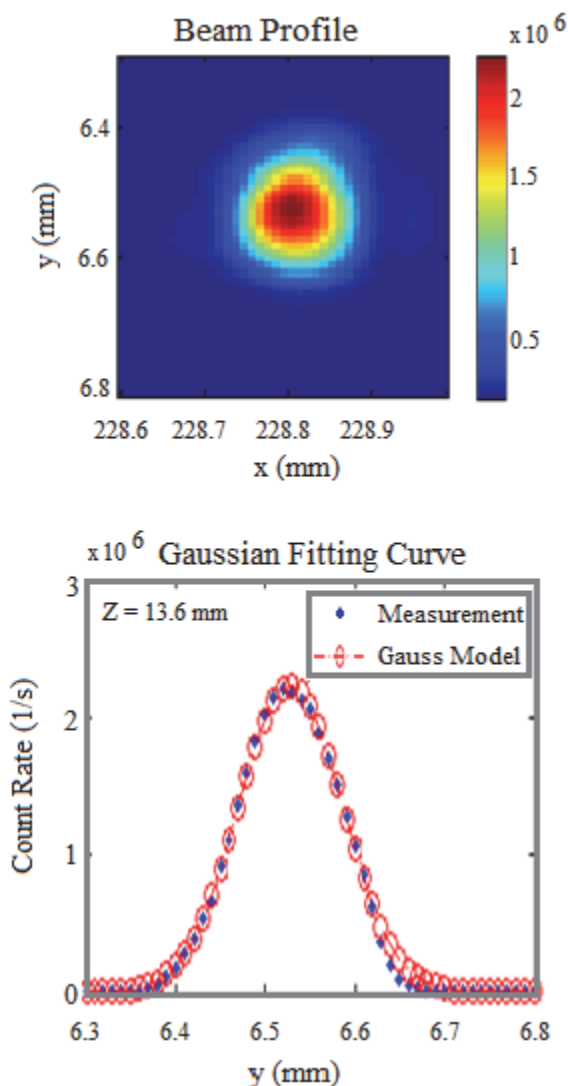


Figure 3.7 Scanning results for the PDM detector at position $Z = 13,6 \text{ mm}$

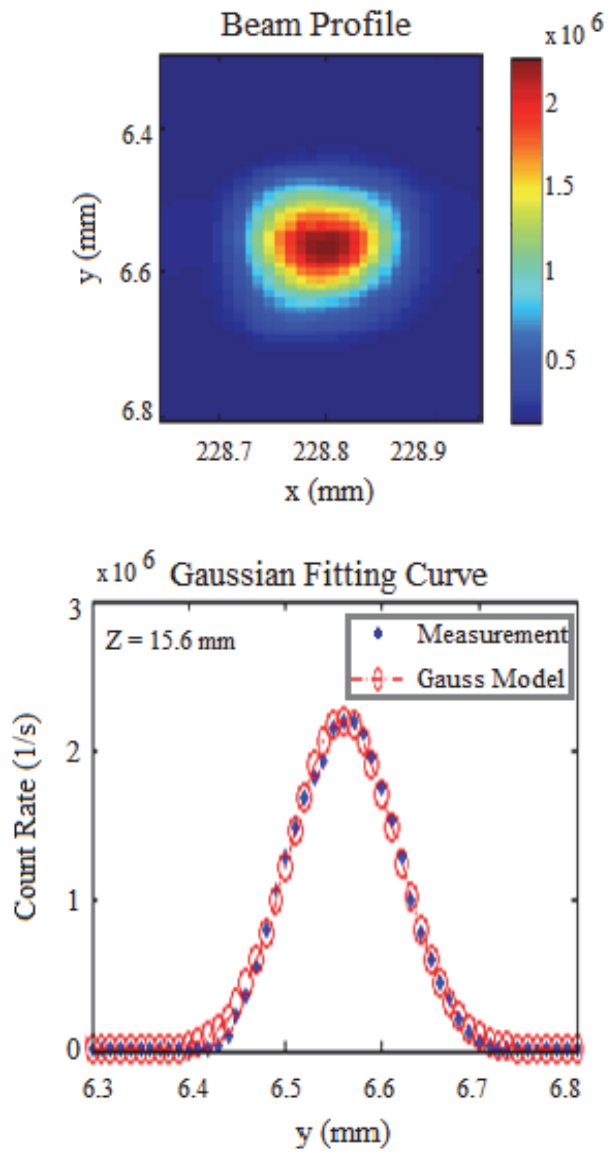


Figure 3.8 Scanning results for the PDM detector at position $Z = 15,6$ mm

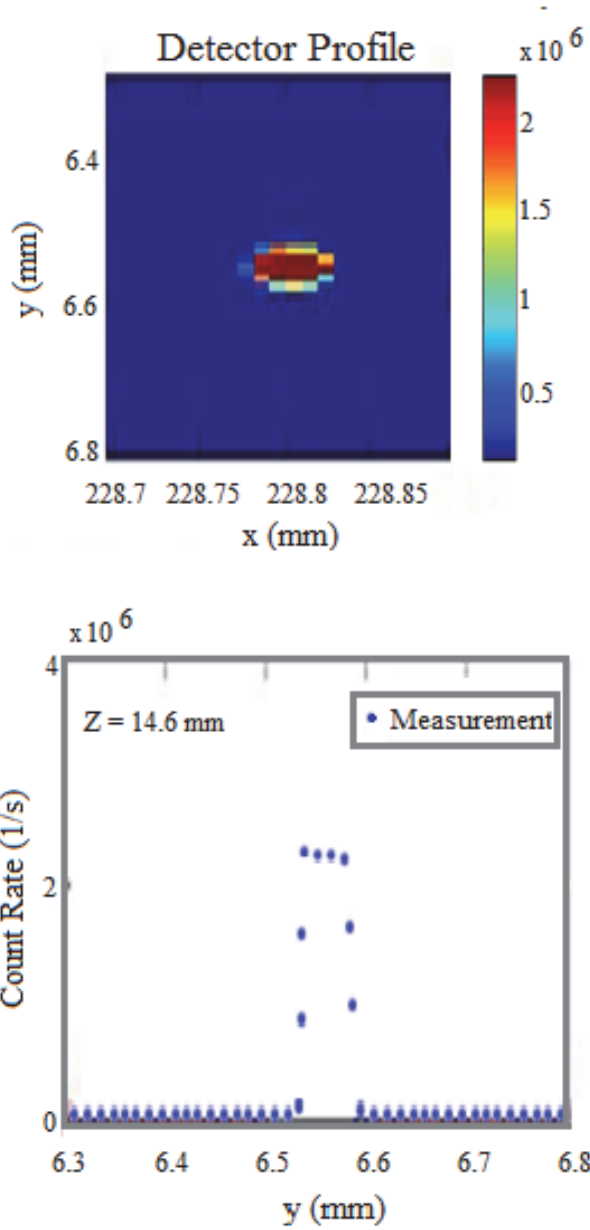


Figure 3.9 Scanning results for the PDM detector at position $Z = 14,6$ mm

Table 3.2. Summary results of the PDM detector

No	Z – position (mm)	x – center (mm)	y – center (mm)	Error (%)	Diameter (mm)
1	13.6	228.81	6.52	7.2	0.23
2	14.6	228.80	6.55	-	0.07
3	15.6	228.79	6.56	7.3	0.23

The same strategy was used to determine precisely the optimal (X, Y, Z) – position of the PDM detector. The results mentioned above have shown that the optimal position is in the (X, Y) - center position of the scan profile with the smallest diameter, i.e. at $x_{\text{center}} = 228,80$ mm, $y_{\text{center}} = 6,55$ mm and $Z = 14,6$ mm.

The results also reveal that the Si-SPAD quantum detection critically depends on the irradiated area and on the beam location in the sensor active area.

3.3.2 Homogeneity studies

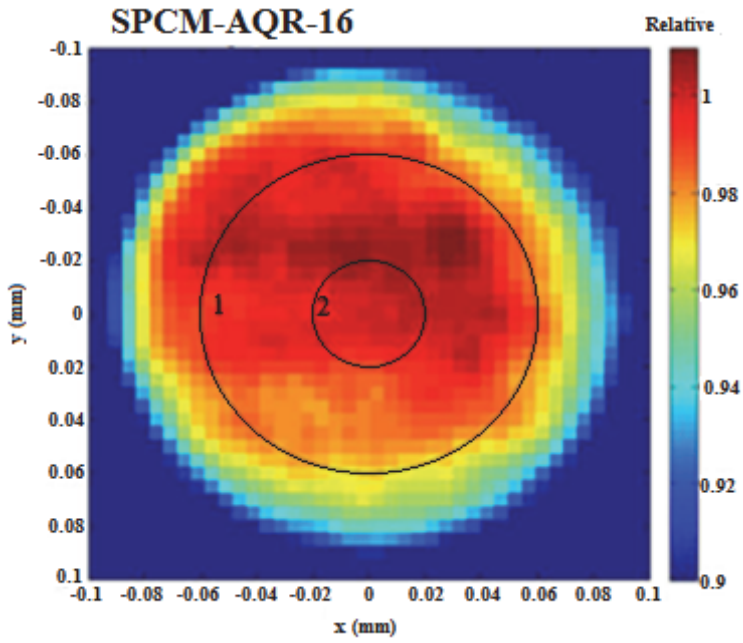
The homogeneity of the Si-SPAD detector was studied as a relative standard deviation (Eq. (3.8)). Homogeneity studies of the detection efficiency of the Si-SPAD detector were conducted at 770 nm laser wavelength, determined by scanning the active area of the Si-SPAD sensor with a laser beam of a diameter of approx. 10 μm . However, in this case, a monitor detector was used for suppressing a possible fluctuation of the laser optical power that may occur during the measurement. The scanning was carried out with a step resolution of 5 μm over the complete active area of the sensor.

It should be noted that only relative measurements are required to determine the homogeneity of the Si-SPAD detection efficiency. Therefore, here each signal obtained from the Si-SPAD for each (x,y) scanning position is normalized to the one obtained when the laser beam is impinging at the center of the sensor active area, i.e.

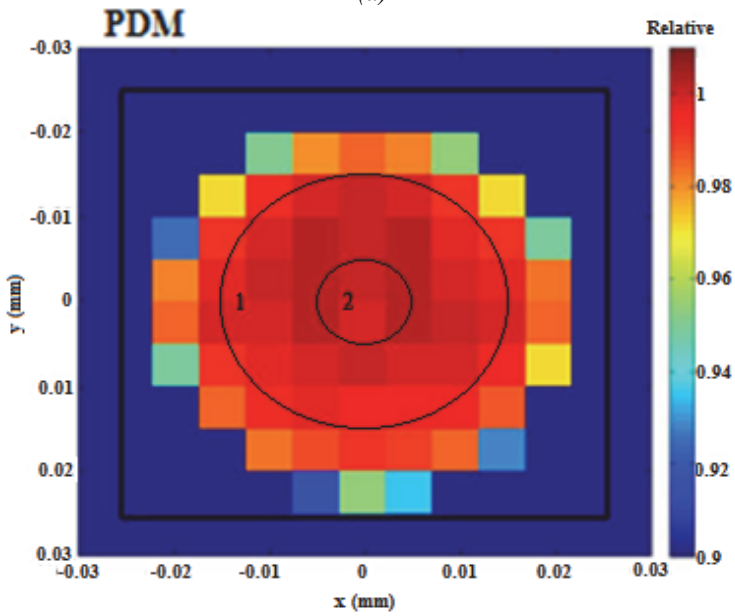
$$N(x, y)_{\text{rel}} = \frac{N_{x_i, y_j}}{N_{\text{center}}} \cdot \frac{s_{\text{mon_center}}}{s_{\text{mon}_{i,j}}}, \quad (3.9)$$

where N_{x_i, y_j} – Si-SPAD counts for the (x, y)-position,
 N_{center} – Si-SPAD count rate at the center position $N_{x=0, y=0}$
 s_{mon} – signal of the monitor detector.

The homogeneity of the detection efficiency may be defined as the relative standard deviation of the relative detection efficiency for a defined region. The summary results for the quantum detection homogeneity of two commercial Si-SPAD detectors are summarized in Table 3.3 and illustrated in Figure 3.10.



(a)



(b)

Figure 3.10 Relative spatial quantum detection efficiency of the Si-SPAD detectors: (a) SPCM-AQR determined with a beam diameter $\phi_B \sim 10 \mu\text{m}$ and circled sensor area with diameter $\phi_{D1} = 180 \mu\text{m}$; (b) PDM determined with a beam diameter $\phi_B \sim 10 \mu\text{m}$ and circled sensor area with diameter $\phi_{D2} = 50 \mu\text{m}$

Table 3.3 Results of the mean value and homogeneity (relative standard deviation) of the Si-SPAD relative detection efficiency for two selected regions of the active area of SPCM-AQR-16 (PerkinElmer) and PDM detectors

Regions	Region Diameter ϕ_{Circle} (μm)	Mean Value (rel.)	Homogeneity RSD
SPCM-AQR-16			
Region 1	120	0.9941	0.85 %
Region 2	40	0.9996	0.34 %
PDM			
Region 1	40	0.9906	2.21 %
Region 2	20	1.009	0.13 %

Figure 3.10 shows the relative spatial responsivity obtained for the Si-SPAD Perkin-Elmer SPCM-AQR-16 and the Micro Photon Devices PDM detector, respectively. As can be observed, for the applied beam diameter of 10 μm , the relative values are within ± 1 % for the main active region of the detectors, however, as expected, at the border of the active regions, the values drop.

To estimate the homogeneity, the standard deviation of the detection efficiency in a specific region of the detector was chosen; see e.g. the circled regions in Figure 3.10. In Figure 3.10 a, the homogeneity of the detection efficiency obtained for the mean detection efficiency within the circled area (region 1) is ≤ 0.85 %. The homogeneity can be improved by selecting smaller regions, i.e. for region 2 with a diameter of 40 μm , the obtained homogeneity is $\leq 0,3$ %. Figure 3.10 b shows the results of the homogeneity studies of the PDM detector. The results reveal that the obtained homogeneity has been improved from $\leq 2,2$ % for region 1 (diameter 40 μm) to $\leq 0,13$ % for region 2 (diameter 20 μm).

Additionally, the relative deviation of the detection efficiency of the Si-SPAD detectors for different beam diameters is shown in Figure 3.11. For this analysis, the relative deviation of the detection efficiency for different beam diameters has been normalized to the detection efficiency obtained for a beam with a diameter of $\phi_B = 20$ μm impinging on the center of the active areas of the Si-SPAD detectors. Figure 3.11 shows that the change of the detection efficiency for different beam diameters originating from the non-perfect homogeneity is larger for the PDM detector than for the PerkinElmer SPCM-AQR-16 detector. However, this behavior is caused by the smaller active area of the PDM detector. The smaller the active area, the more sensitive is the detection efficiency with respect to an increase in the beam diameter. Therefore, in order to compare the sensitivity of the detection efficiency of these two detectors with different beam diameters, the relative detection efficiency as a function of the ratio between the beam diameter and the active area (sensor diameter) is shown in Figure 3.12. Here it is observed that the detection efficiency of the PerkinElmer SPCM-AQR-16 Si-SPAD detector is more sensitive to changes in the beam diameter. These results clearly show that, depending on the active area of the SPAD sensor, an

appropriate laser beam diameter must be used to achieve low measurement uncertainties in the determination of the detection efficiency of a Si-SPAD detector.

The results have shown that homogeneity of the detection efficiency depends on the beam size and the evaluated region.

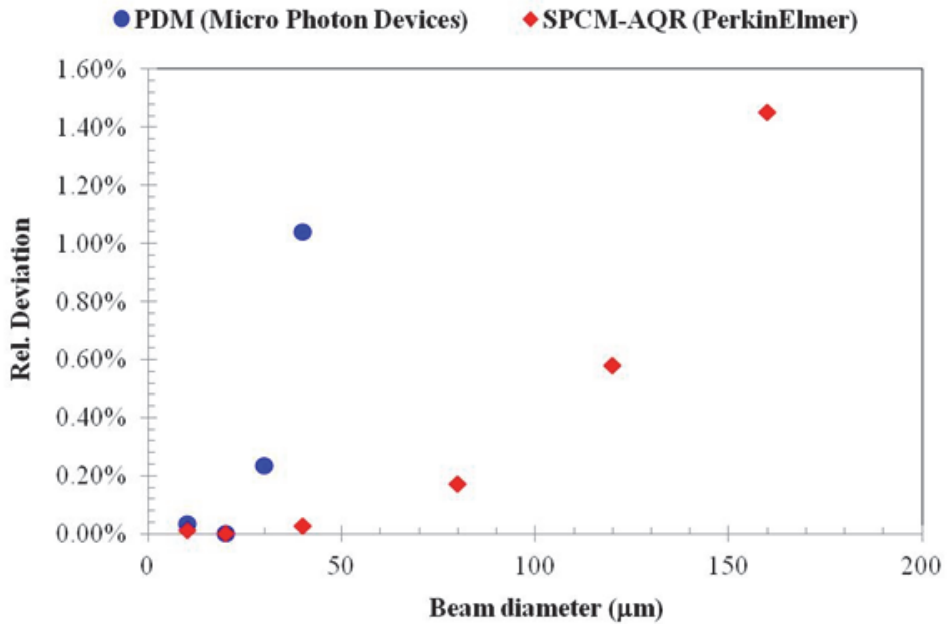


Figure 3.11 Relative deviation of the detection efficiency for different beam diameters at 770 nm laser wavelength

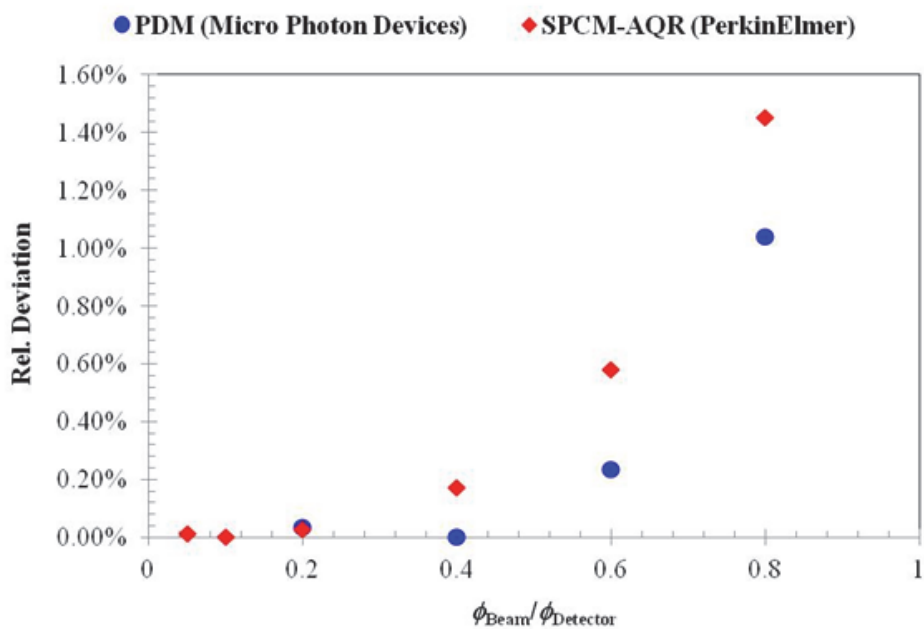


Figure 3.12 Relative deviation in the function of the ratio of beam diameter and beam detector for two commercial Si-SPAD detectors at 770-nm laser wavelength

4. HIGH-ACCURACY FILTER TRANSMISSION MEASUREMENT METHOD FOR CALIBRATION OF THE DETECTION EFFICIENCY OF Si-SPAD DETECTOR

Based on two-photon correlation techniques and on comparison to classically calibrated detectors, absolute detection efficiency of photon-counting devices has been studied for a number of years [40-45]. In this photon correlation technique, traceability is not necessary because in principle, a calibrated standard detector is not needed. However, from a metrological point of view, a validation with a standard detector traceable to the cryogenic radiometer or to a calibrated lamp is necessary, as we can refer to the calibration chain of Figure 1.8 for the determination of the Si-SPAD detection efficiency [36]. The previous research work has stated the problem in improvement of the measurements of the filter transmission which should lead to a significantly reduced measurement uncertainty [36]. Based on it, the current research work will focus on updating a high-accuracy filter transmission measurement method by using integrating sphere for determination the detection efficiency of Si-SPAD detector.

4.1 Measurement method

The measurement method for the determination of the detection efficiency of Si-SPAD detectors is based on the comparison of the Si-SPAD detector count rate with the optical power, i.e. photon flux, measured with a calibrated integrating sphere with attached silicon diode by using the double filter transmission technique [36, 37]. To determine the Si-SPAD detection efficiency by this technique, the transmission of the filters is required to calculate the optical power impinging on the Si-SPAD detector. However, the requirement of a very low filter transmission makes the direct measurement by an analogue detector impossible; thus, a two-step measurement procedure for the filter transmission determination has been developed at PTB, as can be seen in Figure 4.1.

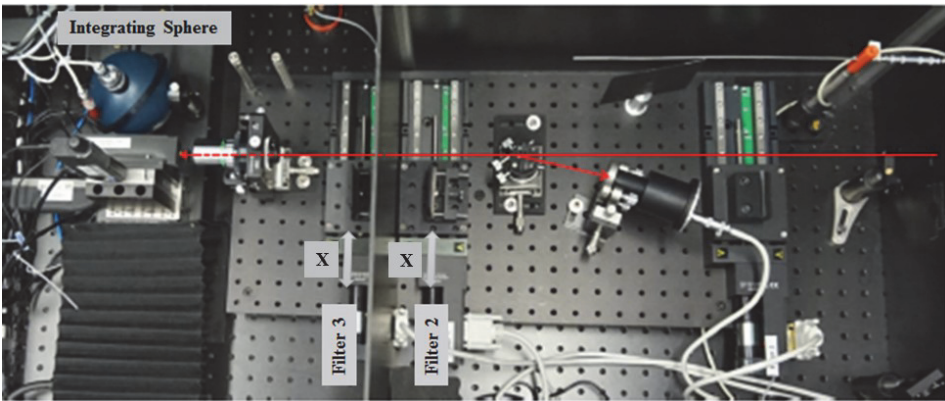
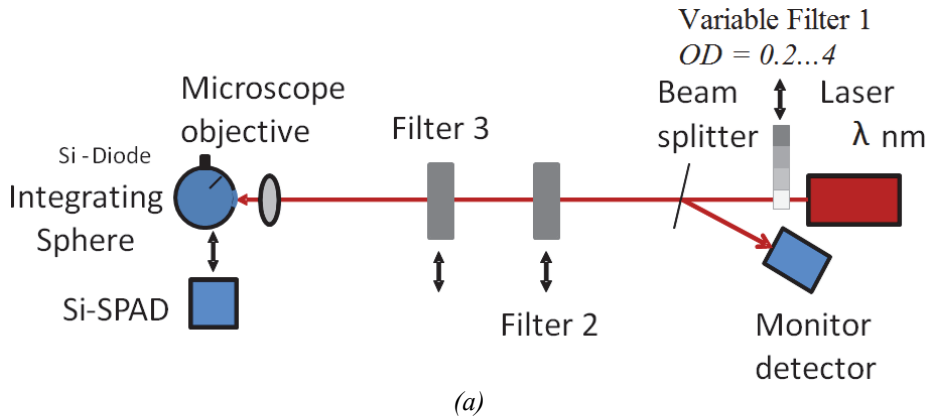


Figure 4.1 New configuration setup for Si-SPAD detector calibration at PTB: (a) Schematic view for the calibration of the detection efficiency of Si-SPAD; (b) Top view illustration setup pictures for the determination of the detection efficiency of Si-SPAD detectors by using an integrating sphere with an attached Si-Diode

A tunable laser source with a wavelength range from 766 nm to 781 nm was used. The laser beam is focused through a microscope objective APO M-PLAN 20x with a 0,42 numerical aperture and a working distance of 20 mm. In the measurement, we used a neutral density filter NG9 D 2.6 for Filter 2 and neutral density filter NG9 D 3.0 for Filter 3. The total transmittances for Filter 2 and Filter 3 used in the wavelength ranges mentioned above are shown in the summary results of the Table 4.1.

We have developed the measurement method by using an integrating sphere instead of using a single silicon detector (Si-Diode) for the filter transmission measurement. The use of the integrating sphere with an attached detector has two main advantages:

- 1) The optical power is not sensitive to the beam size used during the calibration.
- 2) Specular reflections that may occur between the objective lens and the detection system were strongly minimized.

Thus, these advantages will minimize any systematic error for the filter transmission measurement. Figure 4.2 shows a schematic illustration of the integrating sphere with an attached detector.

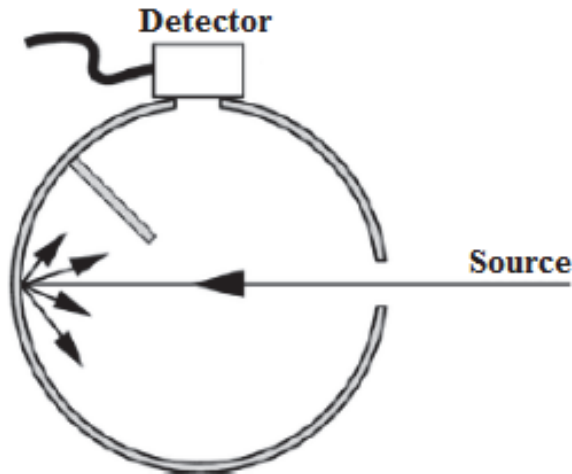


Figure 4.2 Schematic view of the integrating sphere with an attached detector

The integrating sphere with a diameter of 101,6 mm is coated with spectralon and a Si photodiode is attached to one port. The absolute responsivity of the sphere is calibrated against a trap detector traceable to a cryogenic radiometer.

The filter transmission was measured individually for each filter ($T_{\text{Filter}2}$, $T_{\text{Filter}3}$) by using high accuracy translation position stages and the filter transmission of the two filters was measured as a filter package (T_{Combined}). An Agilent VEE program was used to realize automated measurements, as can be seen in the flowchart fragment in Figure 4.3. The measurement program is composed of four modules.

All the modules were connected to each other for the entire measurement procedure. The signals of the integrating sphere and the monitor detector were taken from the readings of two digital multi-meters, which will play an important role in the determination of the filter transmission [36]. The main view of the flowchart of Agilent Vee program shows that the measurement setup is composed of two translation stages.

The first translation stage was used to identify the filter transmission position and the second to identify the position of the integrating sphere. After alignment

into the beam path, the position of the integrating sphere is stationary during the whole measurement procedure. In module 1, the optical power is measured with the integrating sphere without any filter transmission with initial positions ($X_{\text{Filter1}} = 0$ mm, $X_{\text{Filter2}} = 0$ mm and $X_{\text{Filter3}} = 0$ mm). The second measurement step means that to switch to module 2, a time interval of 35 seconds was needed to wait for Filter 2 positioning ($X_{\text{Filter2}} = 37$ mm) in the beam path. The delayed time is related to the movement time of the filters through the translation stage from the initial position to the beam path and vice versa. The waiting time to switch from one module to the other was kept the same in every step of the measurement procedure. The third block view is related to the measurement of module 3, which continues with the individual filters by moving Filter 2 and Filter 3 to different positions ($X_{\text{Filter2}} = 0$ mm and $X_{\text{Filter3}} = 37$ mm). The fourth view is focused in module 4 to complete the measurement procedure by measuring the total filter transmission while Filter 2 and Filter 3 were positioned in the beam path simultaneously ($X_{\text{Filter2}} = 37$ mm and $X_{\text{Filter3}} = 37$ mm). Totally, 100 measurements for a single wavelength were realized. The procedure was the same for each wavelength used in this research work.

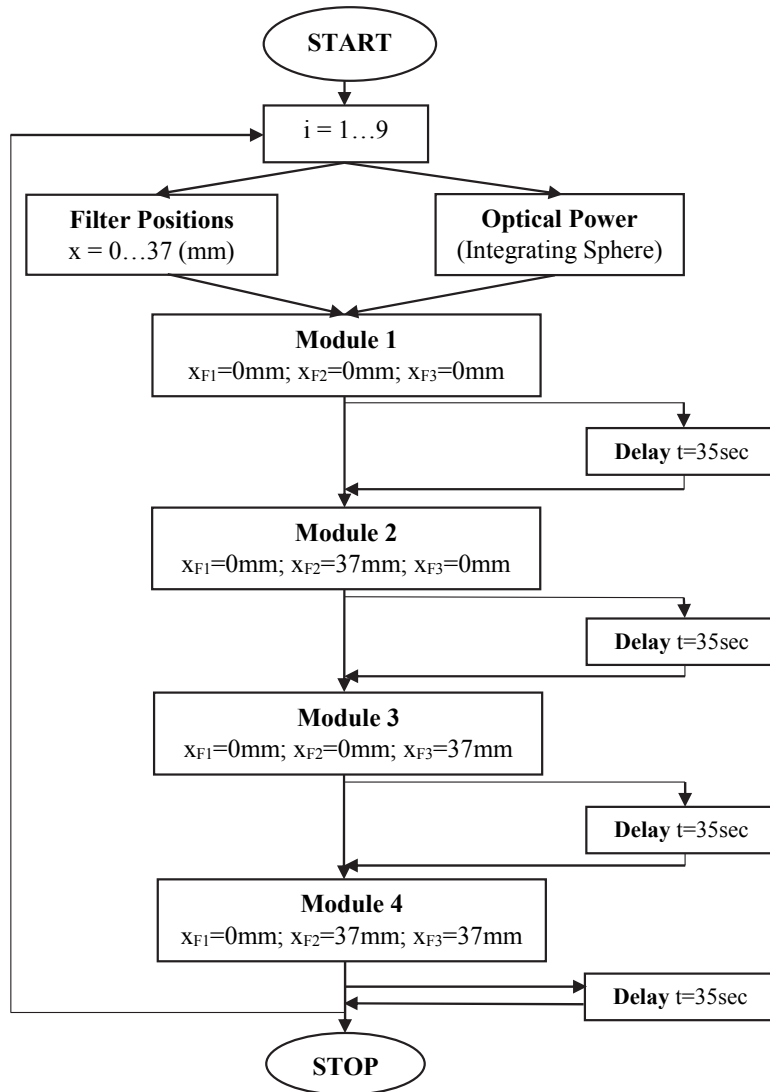


Figure 4.3 Flowchart of the filter transmission measurement by Agilent Vee program

4.2 Measurement model

The measurement model can be expressed as follows in accordance with [32]:

$$y = x + \sum_{i=1}^n \delta x_i, \quad (4.1)$$

where y – estimate of the output quantity,
 x – measured value (detection efficiency of the SPAD),
 δx_i – corrections that arise from input quantities.

According to [36], the measurement model for the determination of the detection efficiency of the Si-SPAD accompanied with all possible contribution factors based on Eq. (4.2) is expressed in Eq. (4.3):

$$\eta = \frac{hc}{\lambda} \frac{A_2 A_3}{A_1} \frac{Q_1 Q_4}{Q_2 Q_3} S_{Si} F_{Filt}, \quad (4.2)$$

where η – detection efficiency of the Si-SPAD detector,
 h – Planck constant,
 c – speed of light,
 λ – wavelength,
 A_1 – amplification factor,
 A_2 – amplification factor,
 A_3 – amplification factor,
 Q_1 – signal of the Si-diode attached to the integrating sphere,
 Q_2 – signal of the Si-diode attached to the integrating sphere,
 Q_3 – signal of the Si-diode attached to the integrating sphere,
 Q_4 – ratio of the counter and the monitor detector signal,
 S_{Si} – spectral responsivity of the integrating sphere with an attached Si-Diode,
 F_{Filt} – factor that uses two filters.

and

$$y = \eta + \delta\eta_h + \delta\eta_c + \delta\eta_\lambda + \delta\eta_{A_1} + \delta\eta_{A_2} + \delta\eta_{A_3} + \delta\eta_{Q_1} + \delta\eta_{Q_2} + \delta\eta_{Q_3} + \delta\eta_{Q_4} + \delta\eta_{S_{Si}} + \delta\eta_{F_{Filt}}, \quad (4.3)$$

where $\delta\eta_i$ – corrections from all input quantities.

4.3 Uncertainty evaluation in the detection efficiency and research results

The measurement uncertainty in the detection efficiency of the Si-SPAD detector was evaluated by the following propagation law of uncertainty and uncertainty of input quantities in accordance with [32, 36]. The combined standard uncertainty of uncorrelated input quantities was determined by the following equation:

$$\begin{aligned}
u_c(y) = [c_i^2 \cdot u(\delta\eta_i)^2]^{1/2} = [c_1^2 \cdot u^2(\delta\eta_h) + c_2^2 \cdot u^2(\delta\eta_c) + \\
+ c_3^2 \cdot u^2(\delta\eta_\lambda) + c_4^2 \cdot u^2(\delta\eta_{A_1}) + c_5^2 \cdot u^2(\delta\eta_{A_2}) + c_6^2 \cdot u^2(\delta\eta_{A_3}) + \\
+ c_7^2 \cdot u^2(\delta\eta_{Q_1}) + c_8^2 \cdot u^2(\delta\eta_{Q_2}) + c_9^2 \cdot u^2(\delta\eta_{Q_3}) + c_{10}^2 \cdot u^2(\delta\eta_{Q_4}) + \\
+ c_{11}^2 \cdot u^2(\delta\eta_{S_{Si}}) + c_{12}^2 \cdot u^2(\delta\eta_{F_{Filt}})]^{1/2} \quad (4.4)
\end{aligned}$$

where c_i – sensitivity coefficients for all input quantities,
 $u(\delta\eta_i)$ – standard uncertainty of the input quantities.

Most of the standard uncertainties of the input quantities associated with sensitivity coefficients were determined previously [36]. Focus of this research work is on the quantity of the use of two filters as one of the major contributions of the standard uncertainty.

The deviation between the individual filter measurements and the overall filter combination was evaluated by the following equation:

$$Dev = 1 - \frac{T_{Filter2} \cdot T_{Filter3}}{T_{Combined}} \quad (4.5)$$

This deviation is taken as the overall uncertainty contribution of the filter transmission for the determination of the detection efficiency of Si-SPAD detectors [36].

Table 4.1 and Figure 4.4 shows the maximum deviation of the filter transmission measurements determined by Eq. (4.5) for different wavelength ranges required for the estimation of the standard uncertainty of the correction factor.

Table 4.1 Summary of the filter transmission measurement results and deviations calculated by Eq. (4.5)

Nr	λ (nm)	Filter 2	Filter 3	Combined Filters	Deviation (%)
1	766	0,0186882	0,0086968	0,0001626	0,020
2	768	0,0188345	0,0087792	0,0001654	0,012
3	770	0,0189695	0,0088636	0,0001681	-0,023
4	772	0,0190674	0,0089108	0,0001699	0,016
5	774	0,0191954	0,0089864	0,0001724	-0,044
6	776	0,0193084	0,0090481	0,0001748	0,030
7	778	0,0194161	0,0091136	0,0001769	-0,012
8	780	0,0195284	0,0091665	0,0001791	0,035
9	781	0,0195746	0,0091978	0,0001800	-0,011

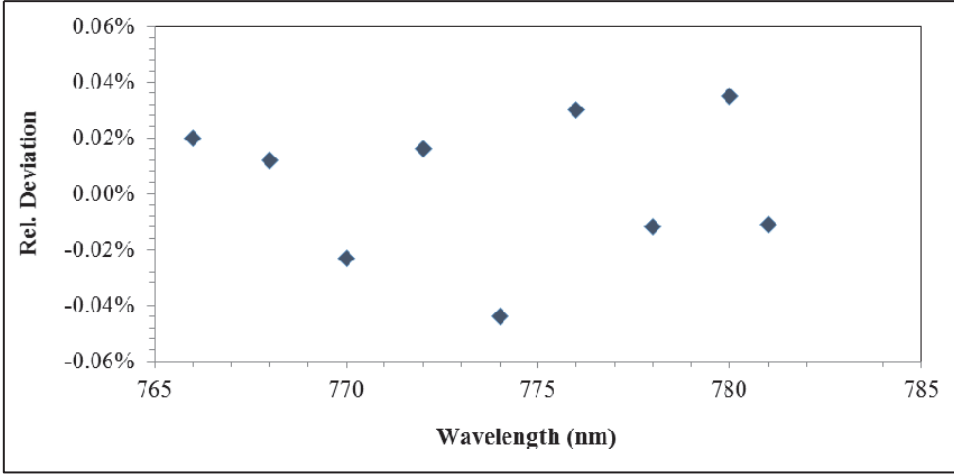


Figure 4.4 Deviation of the filter transmission measurements calculated by Eq. (4.5) for different wavelengths

Based on the results presented in Table 4.1 and Figure 4.4, the standard uncertainty due to the correction factor that arises from two filters was chosen from the largest deviation of approximately 0,05 %, resulting from the transmission measurements at $\lambda=774$ nm. It is expressed by the following equation:

$$u(\delta\eta_{F_{\text{filt}}}) = \frac{T_{\text{Individual}} - T_{\text{Combined}}}{T_{\text{Combined}} \cdot \sqrt{3}} = \frac{(T_{\text{Filter2}} \cdot T_{\text{Filter3}}) - (T_{\text{Combined}})}{T_{\text{Combined}} \cdot \sqrt{3}}, \quad (4.6)$$

where $T_{\text{Filter2}}, T_{\text{Filter3}}$ – filter transmission of each individual filter,
 T_{Combined} – filter transmission of a combined filter.

The sensitivity coefficient was evaluated through the partial derivative of Eq. (4.2) expressed as follows:

$$c_{12} = \frac{\partial \eta}{\partial F_{\text{filt}}} = \frac{hc}{\lambda} \frac{A_2 A_3}{A_1} \frac{Q_1 Q_4}{Q_2 Q_3} S_{\text{Si}}. \quad (4.7)$$

The uncertainty contribution of the factor which uses two filters is expressed by the following equation:

$$u_c(F_{\text{filt}}) = (c_{12}^2 \cdot u_{12}^2)^{1/2} \quad (4.8)$$

The updated measurement uncertainty budget for this improved measurement setup is shown in Table 4.2.

Table 4.2 Measurement uncertainty budget for the determination of the detection efficiency

Uncertainty components	Uncertainty (%)
Planck constant, h	$2,52 \times 10^{-7}$
Speed of light, c	0,0
Wavelength, λ	0,0075
Amplification factor, A_1	0,0021
Amplification factor, A_2	$2,08 \times 10^{-6}$
Amplification factor, A_3	$2,08 \times 10^{-6}$
Ratio V_1/V_{Mon1} , Q_1	0,004
Ratio V_2/V_{Mon2} , Q_2	0,015
Ratio V_3/V_{Mon3} , Q_3	0,05
Ratio CR/V_{MonSPAD} , Q_4	0,036
Spectral responsivity of integrating sphere with Si-Diode, s_{Si}	0,15
Factor for the use of two filters, F_{filt}	0,005
Combined uncertainty, u_c	0,16
Expanded uncertainty, $k=2$	0,32

Taking into account all uncertainty components, the detection efficiency of the Si-SPAD detector at 770 nm for a photon rate of approx. 100 000 photons/s and its associated expanded uncertainty is:

$$\eta_{\text{SPAD}} = 0,5968 \pm 0,32 \% , (k = 2)$$

In comparison to [36] and with reference to our objective targeted to achieve better uncertainty, the results have shown that expanded uncertainty was reduced by a factor of about two. The new configuration setup that was used for the filter transmission measurements has lead to a practically negligible uncertainty contribution due to the factor that uses two filters. Currently, the main contribution is derived from the absolute responsivity calibration of the integrating sphere with the attached detector.

5. CONCLUSIONS

The main objectives of this research work have been gained and two general conclusions can be presented as follows:

Firstly, *an accurate angle measurement method for the mechanical components of a multi-element photodetector and uncertainty estimation were investigated by using the 3D CMM at high accuracy in accordance with the series standards ISO 10360 and GUM.* A measurement and uncertainty estimation model were developed. The sources of uncertainty were described in detail. It was observed that the major uncertainty contribution arises from the reading of indication and repeatability of the measurement results. The developed dimensional measurement method by using the multifunctional 3D CMM allows reliable measurements of the complicated shapes with high accuracy, which can play an important role to ensure the quality of the desired performance of a final product in many modern automation technologies.

Secondly, *a novel method was elaborated and tested to characterize the Si-SPAD detectors and to improve the accuracy of imaging in vision technologies. A measurement model for precise alignment position of Si-SPAD detectors was developed.* The MATLAB-based program was implemented to Agilent Vee program for precise Si-SPAD detector alignment. The quantum detection homogeneity, as one of the key parameters for the characterization of the detection efficiency, depends on the beam size and evaluated region. The quantum detection of the Si-SPAD detector with a large active area is more sensitive to changes in the beam diameters. The determination of the detection efficiency of Si-SPAD detector, as the second key parameter, was improved by using an integrating sphere with the attached detector. The results obtained by using this new configuration setup have shown that one of the major uncertainty contributions due to the filter transmission measurement was reduced by about two times and became practically negligible as compared to other contributions. The improved method for determination of the detection efficiency of Si-SPAD detectors by using filter transmission measurement can play an important role for the accuracy of imaging purpose in vision technologies.

Scientific Novelty

The scientific novelty of the thesis lies in the following:

- An angle measurement method associated with thorough uncertainty estimate can be used for complicated geometrical objects measured at high accuracy by the 3D CMM.
- High accuracy method for the characterization of Silicon Single photon avalanche diode (Si-SPAD) detectors can be used for imaging purposes. It is followed by:

- a. Method for investigation the quantum detection homogeneity study of Si-SPAD detectors.
- b. Using the integration sphere with the attached detector, the accurate filter transmission measurement method has been updated in order to achieve the lowest measurement uncertainty for detection efficiency of the Si-SPAD detectors.

Future research work

During this research work, some ideas and problems that emerged require further investigation as follows:

- Further studies would reveal whether this method can be applied for any angle measurement with lower uncertainty.
- To improve the overall measurement uncertainty of the Si-SPAD detection efficiency, the last major uncertainty contribution resulting from spectral responsivity should be improved.
- New configuration setup needs to be developed or existing updated to improve the uncertainty component that arises from spectral responsivity.

REFERENCES

1. Dotson, L. C., Harlow, R., Thompson, L. R., Busch, T. Fundamentals of Dimensional Metrology, 4th Edition. USA: Measurement/Measuring Instruments, 2003.
2. Gallegos-Funes, F. Vision Sensors and Edge Detection. Croatia: Computer and Information Science, 2010.
3. Pfeifer, T. Production Metrology. Germany: ISBN 3-486-25885-0, 2002.
4. Solari, F. R., Chessa, M., Sabatini, S. P. Machine Vision – Applications and Systems. Croatia: ISBN 978-953-51-0373-8, 2012.
5. Batchelor, G. B., Whelan, F. P. Intelligent Vision System for Industry, UK: ISBN-13 978-1447111405, 2002.
6. Photonics Catalogue [WWW]
http://www.photonics21.org/download/FinalEditionPhotonics21VisionDocument_InternetVersion.pdf
(01.05.2015)
7. Hocken, J. R., Pereira, H. P. Coordinate Measuring Machines and Systems. USA: Manufacturing Engineering and Material Processing, 2011.
8. Radhakrishnan, J. Computer Numerical Control Machines and Computer Aided Manufacture, first ed., Coimbatore, Tamil Nadu, 2012.
9. Geometrical Product Specifications (GPS) - Acceptance and Reverification Tests for Coordinate Measuring Machines (CMM) - Part 2: ISO 10360-2. CMMs Used for Measuring Linear Dimensions, 2009.
10. Geometrical product specifications (GPS) - Acceptance and Reverification Tests for Coordinate Measuring Machines (CMM) - Part 3: ISO 10360-3. CMMs with the Axis of a Rotary Table as the Fourth Axis, 2000.
11. Geometrical Product Specifications (GPS) - Acceptance and Reverification Tests for Coordinate Measuring Machines (CMM) - Part 4: ISO 10360-4. CMMs used in Scanning Measuring Mode, 2000.
12. Geometrical Product Specifications (GPS) - Acceptance and Reverification Tests for Coordinate Measuring Machines (CMM) - Part 5: ISO 10360-5. CMMs using Single and Multiple Stylus Contacting Probing Systems, 2010.
13. Geometrical Product Specifications (GPS) - Acceptance and Reverification Tests for Coordinate Measuring Machines (CMM) - Part 6: ISO 10360-6. Estimation of Errors in Computing Gaussian Associated Features, 2001.
14. Geometrical Product Specifications (GPS) - Acceptance and Reverification Tests for Coordinate Measuring Machines (CMM) - Part 7: ISO 10360-7. CMMs Equipped with Imaging Probing Systems, 2011.
15. Geometrical Product Specifications (GPS) - Acceptance and Reverification Tests for Coordinate Measuring Machines (CMM) - Part 8: ISO/CD 10360-8. CMMs with Optical Distance Sensors, 2011.

16. Geometrical Product Specifications (GPS) - Acceptance and Reverification Tests for Coordinate Measuring Machines (CMM) - Part 9: ISO/DIS 10360-9. CMMs with Multiple Probing Systems, 2011.
17. Geometrical Product Specifications (GPS) - Acceptance and Reverification Tests for Coordinate Measuring Machines (CMM) - Part 10: ISO/FDIS 10360-10. Laser Trackers for Measuring Point-to-Point Distances, 2011.
18. Geometrical Product Specifications (GPS) - Guidelines for the Evaluation of Coordinate Measuring Machine (CMM) Test Uncertainty: DD ISO/TS 23165, 2006.
19. Baldwin, M. J., Summerhays, D. K., Campbell, A. D., Henke, P. R. Application of Simulation Software to Coordinate Measurement Uncertainty Evaluations, *Measure*, 2007, 2, 40-52.
20. Bureau International des Poids et Mesures. – The International System of Units (SI): Paris: BIPM 2006.
21. Van Nieuwenhove, D., Van der Tempel, W., Grootjans, R., Kuijk, M. Time-of-flight Optical Ranging Sensor Based on a Current Assisted Photonic Demodulator, *In: Proceedings Symposium IEEE/LEOS Benelux Chapter, Eindhoven*, 2006, 2009–2012.
22. Li, L. Introduction to Time of Flight Camera, *Technical White Paper of Texas Instruments*, 2014, SLOA190B, 1–10.
23. Lange, R. 3D Time-of-Flight Distance Measurement with Custom Solid-State Image Sensors in CMOS/CCD-technology: Doctoral Thesis, Siegen, University of Siegen, 2000.
24. Hansard, M., Lee, S., Choi, O., Horaud, R. Time-of-Flight Cameras: Principles, Methods and Applications. France: Springer Briefs in Computer Science, 2012.
25. Niclass, L.C. Single-Photon Image Sensors in CMOS: Picosecond Resolution for Three-Dimensional Imaging: Doctoral Thesis, Lausanne, Polytechnic University of Lausanne, 2008.
26. Dongeek, Sh., Kirmani, A., Goyal, K. V., Shapiro, H. J. Photon-Efficient Computational 3D and Reflectivity Imaging with Single-Photon Detectors, *IEEE Transactions on Computational Imaging*. 2015, 1, 112-125.
27. Gallivanoni, A., Rech, I., Resnati, D., Ghioni, M., Cova, S. Monolithic Active Quenching and Picosecond Timing Circuit Suitable for Large-Area Single-Photon Avalanche Diodes, *Optics Express*. 2006, 14, 5021-5030.
28. Xiaobin, X. Design and fabrication of 4H-SiC Detectors towards Single Photon Counting: Doctoral Thesis, New Jersey, Rutgers University, 2007.
29. Vornicu, I., Carmona-Galán, R., Rodríguez-Vázquez, A. A CMOS 8x8 SPAD Array for Time-of-Flight Measurement and Light-Spot Statistics, *In: Proceedings IEEE International Symposium on Circuits and Systems*, 2013, 2626-2629.
30. TESA MICRO-HITE 3D Coordinate Measuring Machine Brochure [WWW] http://swissinstruments.com/downloads/metrology_coordinate.pdf (21.03.2015)

31. Kübarsepp, T., Kärhä, P. and Ikonen, E. Characterization of a Polarization-Independent Transmission Trap Detector, *Applied Optics*, 1997, 36 (13), 2807–2812.
32. Guide to the Expression of Uncertainty in Measurement (GUM). International Standard ISO/IEC Guide 98-3:2008. Geneva: International Organization for Standardization, 2008.
33. D’Amato, R., Caja, J., Maresca, P., Gómez, E. Use of Coordinate Measuring Machine to Measure Angles by Geometric Characterization of Perpendicular Planes- Estimating Uncertainty, *Measurement*, 2014, 47, 598-606.
34. Gisin, N., Ribordy, G., Tittel, W., Zbinden, H. Quantum Cryptography, *Reviews of Modern Physics*, 2002, 74, 145–195.
35. Cova, S., Ghioni, M., Lotito, A., Rech, I., Zappa, F. Evolution and Prospects for Single-Photon Avalanche Diodes and Quenching Circuits, *Journal of Modern Optics*, 2004, 51, 1267–1288.
36. López, M., Hofer, H., Kück, S. Detection Efficiency Calibration of Single-Photon Silicon Avalanche Photodiodes Traceable Using Double Attenuator Technique, *Journal of Modern Optics*, 2015, 62, S21-S27.
37. Kück, S., Hofer, H., Peters, S., López, M. Detection Efficiency Calibration of Silicon Single-Photon Avalanche Diodes Traceable to a National Standard, In: *Proceedings of NEWRAD: 12th International Conference on New Developments and Applications in Optical Radiometry*, Espoo, 2014, 93-94.
38. SPCM-AQR Detector [WWW]
http://www.optics.rochester.edu/workgroups/lukishova/QuantumOpticsLab/hompage/apd_spcm_aqr.PDF (15.11.2015)
39. PDM Detector [WWW]
<http://www.micro-photon-devices.com/Docs/Datasheet/PDM.pdf> (15.11.2015)
40. Chunnillal, Ch. J., Degiovanni, I. P., Kück, S., Müller I., Sinclair, A. G. Metrology of Single-Photon Sources and Detectors: A Review, *Optical Engineering*, 2014, 53, 01-17.
41. Ghazi-Bellouati, A., Razet, A., Bastie, J., Himbert, M. E., Degiovanni, I. P., Castelletto, S., Rastello, M. L. Radiometric Reference for Weak Radiations: Comparison of Methods, *Metrologia*, 2005, 42, 271-277.
42. Müller, I., Klein, R. M., Hollandt, J., Ulm, G., Werner, L. Traceable Calibration of Si Avalanche Photodiodes Using Synchrotron Radiation, *Metrologia*, 2014, 49, S152.
43. Migdall, A.; Polyakov, S.V.; Fan, J.; Bienfang, J.C. Single-Photon Generation and Detection, Physics and Applications (Experimental Methods in the Physical Sciences), ISBN-13: 978-0123876959, ISBN-10: 0123876958; Watham, MA: *Academic Press*, 45, 2013.
44. Kwiat, P.G., Steinberg, A.M., Chiao, R.Y., Eberhard, P.H., and Petroff, M.D. High-Efficiency Single-Photon Detectors, *Physical Review A*, 1993, 48, R867–R870.

45. Migdall, A.L.; Datla, R.U.; Sergienko, A.; Shih, Y.H. Absolute Detector Quantum-Efficiency Measurements Using Correlated Photons, *Metrologia*, 1996, 32, 479–483
46. Yandayan, T.; Akgoz, S.A.; Haitjema, H. A novel technique for calibration of polygon angles with non-integer subdivision of indexing table, *Precision Engineering*, 2002, 26 (4), 412–424.
47. Pekelsky, R.J.; Munro, E. L. Bootstrap calibration of an autocollimator, index table and sine bar ensemble for angle metrology, In: *Proc. SPIE 5879, Recent Developments in Traceable Dimensional Measurements III*, California, 2005, 58790D.
48. Yandayan, T.; Ozgur, B.; Karaboce, N.; Yaman, O. High precision small angle generator for realization of the SI unit of plane angle and calibration of high precision autocollimators, *Measurement Science and Technology*, 2012, 23 (9), 1–12.
49. Yau H.; Menq, C. An automated dimensional inspection environment for manufactured parts using co-ordinate measuring machines, *International Journal of Production and Research*, 1992, 30 (7), 1517-1536.
50. Gao, H.C.; Cheng, K.; Webb, D. Investigation on the sampling size optimization in gear tooth surface measurement using a CMM, *International Journal of Advanced Manufacturing Technology*, 2004, 24 (7), 599-606.
51. Tyler Estler, W. Uncertainty Analysis for Angle Calibrations Using Circle Closure, *Journal of Research of the National Institute of Standards and Technology*, 1998, 103, 141-151.
52. T. Matsuda and M. Kajitani, An automatic calibration system for angular encoders, *Prec. Eng.*, 1989, 11, 95–100.
53. Chapman, V.A.M; Fergusson-Kelly, R.; Holloway, A.; Lee, W. Interferometric angle measurement and the hardware options available from Renishaw, *Technical white paper*, 2013, TE326, 1–17.
54. Stone, J.; Muralikrishnan, B. Geometric Effects When Measuring Small Holes With Micro Contact Probes, *Journal of Research of the National Institute of Standards and Technology*, 2011, 116, 573–587.
55. B. Muralikrishnan, J. Stone and J. Stoup, Fiber Deflection Probe for Small Hole Metrology, *Precision Eng.—J. Int. Soc.Prec.Eng. Nanotechnol.* 2006, 30, 154-164.

LIST OF PUBLICATIONS

1. **Dhoska, K.;** Hofer, H.; López, M.; Rodiek, B.; Kübarsepp, T.; Kück, S. (2016). Detection efficiency calibration of Si-SPAD detectors via comparison with a Si-Standard diode. *11th International Conference of DAAAM Baltic, Industrial Engineering*, Tallinn, Estonia, [In Press].
2. **Dhoska, K.;** Hofer, H.; López, M.; Kübarsepp, T.; Kück, S (2015). Alignment position method for SPAD detector calibration and homogeneity. *International Journal of Scientific Reports, Medip Academy*, vol. 1(7), pp. 271 - 274.
3. **Dhoska, K.;** Kübarsepp, T.; Dorri, A.; Pramono, A. (2015). Metrological Overview for Coordinate Measuring Machines. *Scientific Journal in Applied Mechanics and Materials, Trans Tech Publications*, vol. 771, pp. 195 - 199.
4. **Dhoska, K.;** Hofer, H.; López, M.; Rodiek, B.; Kübarsepp, T.; Kück, S. (2015). High accuracy filter transmission measurement for determination of the detection efficiency calibration of Si-SPAD detector. *10th International Conference of DAAAM Baltic, Industrial Engineering*, Tallinn, Estonia, pp. 123 - 127.
5. **Dhoska, K.;** Kübarsepp, T.; Hermaste, A. (2014). Uncertainty evaluation of angle measurements by using 3d coordinate measuring machine. *9th International Conference of DAAAM Baltic, Industrial Engineering*, Tallinn, Estonia, pp. 221 - 225.

OTHER PUBLICATIONS

1. Rodiek, B.; López, M.; Hofer, H.; **Dhoska, K.**; Kück, S. (2015). Double Scanning Confocal Microscope for the Characterization of Single-photon Emitters. *7th International Conference on Single-Photon Technologies, SPW2015*, Geneva, Switzerland, [in Press].
2. López, M.; **Dhoska, K.**; Hofer, H.; Rodiek, B.; Kübarsepp, T.; Kück, S. (2015). Measurement of the quantum detection homogeneity of Si-SPAD detectors. *7th International Conference on Single-Photon Technologies, SPW2015*, Geneva, Switzerland, [in Press].
3. López, M.; **Dhoska, K.**; Hofer, H.; Rodiek, B.; Kübarsepp, T.; Kück, S. (2015). High-accuracy measurement of the detection efficiency of Si-SPAD detectors using double attenuator technique. *7th International Conference on Single-Photon Technologies, SPW2015*, Geneva, Switzerland, [in Press].
4. **Dhoska, K.**; Hofer, H.; López, M.; Kübarsepp, T.; Kück, S. (2015). Optimization of the Alignment Position for SPAD detector Calibration. *15th International Symposium "Topical Problems In The Field Of Electrical And Power Engineering" and "Doctoral School of Energy and Geotechnology II"*, Pärnu, Estonia, January 12 - 16, pp. 201 - 202. Tallinn University of Technology
5. Kübarsepp, T.; A. Pokatilov, A.; Vabson, V.; **Dhoska, K.**; Porrovecchio, G.; Göttinger, S.; Manninen, A.; Kück, S. (2014). High-attenuation tunnel-type detector for calibration of single-photon devices. *12th International Conference on New Developments and Applications in Optical Radiometry, Instrumentation and Measurement*, Espoo, Finland, pp. 115 - 116.
6. **Dhoska, K.**; Vabson, V.; Hermaste, A.; Kübarsepp, T. (2014). Dimensional Accuracy for Multi-element Photodetector. *12th International Conference on New Developments and Applications in Optical Radiometry, Instrumentation and Measurement*, Espoo, Finland, pp. 352.
7. **Dhoska, K.**; Kübarsepp, T.; Hermaste, A. (2014). 3D Measurement Setup for Angle Measurement Multi-element Photo-detector. *14th International Symposium "Topical Problems In The Field Of Electrical And Power Engineering" and "Doctoral School of Energy and Geotechnology II"*, Pärnu, Estonia, January 13 - 17, pp. 256 - 258.
8. **Dhoska, K.**; Kübarsepp, T. (2013). Metrological Problem Mapping for Coordinate Measuring Machines. *13th International Symposium "Topical*

Problems in the Field of Electrical and Power Engineering", Doctoral School of Energy and Geotechnology. Pärnu, Estonia, January 14 - 18, pp. 312 - 316.

ACKNOWLEDGEMENTS

Firstly, I would like to thank my supervisor Prof. Toomas Kübarsepp for his support and excellent guidance all through my research work. Without his help, encouragement, discussion and opening opportunities for research work at TUT and outside Estonia at PTB (German National Institute of Metrology), it would not have been possible to finish this research work in good time.

Secondly, I would like to thank all the PTB colleagues starting from Prof. Stefan Kück, Dr. Marco López, engineer Helmuth Hofer, and PhD student Beatrice Rodiek for their collaboration and contribution to these studies.

Special thanks for the Rector of the Polytechnic University of Tirana Academician Jorgaq Kacani for his support in my academic career. I would like to thank my colleagues PhD student Aigar Hermaste from Tallinn University of Technology, PhD student Lorenc Malka, PhD student Alfred Daci and Assoc. Prof. Altin Dorri from Polytechnic University of Tirana, PhD student Agus Pramono from University of Sultan Ageng Tirtayasa for their contribution to this research. Also, I would like to thank Mrs. Mare-Anne Laane for revising and editing English texts in my thesis.

Thirdly, I appreciate gratefully European Metrology Research Program with a project Single-Photon Sources for Quantum Technology (SIQUTE) and Researcher Mobility Grant (RMG) EXL01-RMG1, Estonian Government, Metrosert AS and Mechatronics Department of TUT for financial resources and support of this study. Additionally, I would like to thank all my colleagues from the Department of Mechatronics who created a pleasant atmosphere and environment for my study and life here.

Fourthly, my special thanks are due to my family, relatives, friends and workmates for their support, motivation and optimism during the whole doctoral study period.

Finally, I would like to thank GOD for many blessings made to me during this time that have made everything to work in a perfect way.

ABSTRACT

“Measurement methods with 3D Coordinate Measuring Machine and improved characterization setup for detector performance”

The present thesis is focused on the state-of-the-art in metrology used for the 3D CMM by measuring a complicated geometrical object and on the characterization of the Silicon Single Photon Diode (Si-SPAD) detectors as a key component that would provide accuracy of imaging in Machine Vision.

In accordance with the main objectives of this research work, the following tasks were developed:

- Literature review with a focus on the nature of the 3D Coordinate Measuring Machine (CMM) Metrology and Single Photon Avalanche Diode (SPAD) detectors used for imaging purposes in Machine Vision.
- Development of the measurement model for dimensional accuracy measurement, in particular angle measurement for a complicated geometrical object, such as a three-element photodetector by using the 3D CMM.
- Development of the position alignment procedure for precise Si-SPAD detector calibration and investigation of the quantum detection homogeneity.
- Updating of the existing accurate filter transmission measurement method for calibration of detection efficiency of Si-SPAD detectors. New configuration setup was developed to improve measurements of the detection efficiency of the Si-SPAD detector and uncertainty was reduced by about two times.

In general terms, this research work proposes novel measurement models and calibration methods for dimensional accuracy of complicated measurement shapes and detection efficiency of Si-SPAD detectors. Every significant measurement in this study is traceable to SI units and is accompanied with a stated measurement uncertainty.

KOKKUVÕTE

“Mõõtemetodid detektori toimimise iseloomustamiseks 3D-koordinaatmõõtemasinaga ja arendatud mõõteskeemiga”

Antud töös keskendub autor nüüdisaegse metroloogia rakendusvõimaluste uurimisele mõõtetehnoloogiates, mida kasutatakse 3D-koordinaatmõõtemasinas keeruliste geomeetriliste objektide mõõtmete määramisel ning räni-põhiste üksikfootonidetektorite (Si-SPAD) kui masinnägemise kujutise loomisel täpsust tagavate võtmekomponentide iseloomustamisel.

Vastavalt töö põhieesmärkidele on see jagatud järgmisteks osadeks:

- Kirjanduse analüüs, mis keskendub 3D-koordinaatmõõtemasina metroloogiale ja SPAD detektoritele, mida kasutatakse masinnägemisel kujutise loomiseks.
- Mõõtemudeli väljatöötamine mõõtemääramatuse hindamiseks nurkade mõõtmisel keerukate objektide puhul, kasutades 3D-koordinaatmõõtemasinat.
- Positsiooni justeerimise protseduuri väljatöötamine Si-SPAD detektori täpseks kalibreerimiseks ja analoogsete detektorite kvantdetekteerimise pinnaühtluse uurimiseks.
- Filtrite läbilaskvuse mõõtmise parandamine Si-SPAD detektorite kvantefektiivsuse määramisel. Olemasolevat kalibreerimise süsteemi täiendati, mille tulemusel mõõtemääramatus vähenes umbes kaks korda.

Antud uurimistöö pakub uudseid mõõtemudeleid ja kalibreerimismeetodeid keeruliste uuritavate geomeetriliste objektide mõõtmise täpsuse tõstmiseks ja Si-SPAD detektorite kvantefektiivsuse mõõtemääramatuse vähendamiseks. Iga oluline mõõtetulemus antud töös on seostatud SI-ühikutega ja on esitatud koos vastava mõõtemääramatuse hinnanguga.

ELULOOKIRJELDUS

1. Isikuandmed

Ees- ja perekonnanimi Klodian Dhoska
Sünniaeg ja -koht 25. mai 1983, Tirana
Kodakondsus Albaania

2. Kontaktandmed

Address Ehitajate tee 5, 19086 Tallinn
Telefon +372 58535831, +355 692107333
E-post klodian.dhoska@ttu.ee

3. Hariduskäik

Õppeasutus (nimetus lõpetamise ajal)	Lõpetamise aeg	Haridus (eriala/kraad)
Tartu Ülikool	2008 - 2010	Rakenduslik mõõteteadus (M.Sc.)
Polütehniline Ülikool Tirana	2001 - 2007	Mehaanikateaduskond (Dipl.-Ing)
Ismail Qemali Gümnaasium	1998 - 2001	(keskharidus)

4. Keelteoskus (alg-, kesk- või kõrgtase)

Keel	Tase
Albaania keel	kõrgtase
Inglise keel	kõrgtase
Itaalia keel	kõrgtase
Eesti keel	algtase
Vene keel	algtase

5. Teenistuskäik

Töötamise aeg	Tööandja nimetus	Ametikoht
2014 -	PTB, Rahvusvaheline Metroloogia Instituut Saksamaa	Külasteadur

2014 -	Albaania Akrediteerimisdirektoraat	Tehniline assessor
2012 -	Tallinna Tehnikaülikool, Mehhatroonikainstituut	Nooremteadur
2011 - 2014	Albaania Akrediteerimisdirektoraat	Tehniline ekspert
2011 - 2012	Polütehniline Ülikool Tirana	Lektor
2010 - 2012	Vitrina Ülikooli Mehhatroonikainstituut ja Telekommunikatsioon	Osakonna juhataja
2007 - 2008	Albaania Akrediteerimisdirektoraat	Spetsialist

CURRICULUM VITAE

1. Personal data

Name Klodian Dhoska
Date and place of birth 25 May 1983 Tirana, Albania

2. Contact information

Address Ehitajate tee 5, 19086 Tallinn
Phone +372 58535831, +355 692107333
E-mail klodian.dhoska@ttu.ee

3. Education

Educational institution	Graduation year	Education (field of study/degree)
University of Tartu	2008 - 2010	Applied Measurement Science, (M.Sc.)
Polytechnic University of Tirana	2001 - 2007	Mechanical Engineering diploma study (Dipl.-Ing)
Ismail Qemali High School	1998 - 2001	(High School Education)

4. Language competence/skills (fluent, average, basic skills)

Language	Level
Albanian	fluent
English	fluent
Italian	fluent
Estonian	basic skills
Russian	basic skills

5. Professional Employment

Period	Organization	Position
2014 - present	PTB, National Metrology Institute of Germany	Guest Researcher
2014 - present	Albanian Accreditation Directorate	Technical Assessor

2012 - present	Tallinn Univ. of Technology, Dept. of Mechatronics	Early Stage Researcher
2011 - 2014	Albanian Accreditation Directorate	Technical Expert
2011 - 2012	Polytechnic University of Tirana	Lecturer
2010 - 2012	Vitrina University, Dept. of Mechatronics and Telecommunications	Head of Department
2007 - 2008	Albanian Accreditation Directorate	Specialist

**DISSERTATIONS DEFENDED AT
TALLINN UNIVERSITY OF TECHNOLOGY ON
*MECHANICAL ENGINEERING***

1. **Jakob Kübarsepp**. Steel-Bonded Hardmetals. 1992.
2. **Jakub Kõo**. Determination of Residual Stresses in Coatings & Coated Parts. 1994.
3. **Mart Tamre**. Tribocharacteristics of Journal Bearings Unlocated Axis. 1995.
4. **Paul Kallas**. Abrasive Erosion of Powder Materials. 1996.
5. **Jüri Pirso**. Titanium and Chromium Carbide Based Cermets. 1996.
6. **Heinrich Reshetnyak**. Hard Metals Serviceability in Sheet Metal Forming Operations. 1996.
7. **Arvi Kruusing**. Magnetic Microdevices and Their Fabrication methods. 1997.
8. **Roberto Carmona Davila**. Some Contributions to the Quality Control in Motor Car Industry. 1999.
9. **Harri Annuka**. Characterization and Application of TiC-Based Iron Alloys Bonded Cermets. 1999.
10. **Irina Hussainova**. Investigation of Particle-Wall Collision and Erosion Prediction. 1999.
11. **Edi Kulderknup**. Reliability and Uncertainty of Quality Measurement. 2000.
12. **Vitali Podgurski**. Laser Ablation and Thermal Evaporation of Thin Films and Structures. 2001.
13. **Igor Penkov**. Strength Investigation of Threaded Joints Under Static and Dynamic Loading. 2001.
14. **Martin Eerme**. Structural Modelling of Engineering Products and Realisation of Computer-Based Environment for Product Development. 2001.
15. **Toivo Tähemaa**. Assurance of Synergy and Competitive Dependability at Non-Safety-Critical Mechatronics Systems design. 2002.
16. **Jüri Resev**. Virtual Differential as Torque Distribution Control Unit in Automotive Propulsion Systems. 2002.
17. **Toomas Pihl**. Powder Coatings for Abrasive Wear. 2002.
18. **Sergei Letunovitš**. Tribology of Fine-Grained Cermets. 2003.
19. **Tatyana Karaulova**. Development of the Modelling Tool for the Analysis of the Production Process and its Entities for the SME. 2004.
20. **Grigori Nekrassov**. Development of an Intelligent Integrated Environment for Computer. 2004.
21. **Sergei Zimakov**. Novel Wear Resistant WC-Based Thermal Sprayed Coatings. 2004.
22. **Irina Preis**. Fatigue Performance and Mechanical Reliability of Cemented Carbides. 2004.
23. **Medhat Hussainov**. Effect of Solid Particles on Turbulence of Gas in Two-Phase Flows. 2005.
24. **Frid Kaljas**. Synergy-Based Approach to Design of the Interdisciplinary Systems. 2005.

25. **Dmitri Neshumayev.** Experimental and Numerical Investigation of Combined Heat Transfer Enhancement Technique in Gas-Heated Channels. 2005.
26. **Renno Veinthal.** Characterization and Modelling of Erosion Wear of Powder Composite Materials and Coatings. 2005.
27. **Sergei Tisler.** Deposition of Solid Particles from Aerosol Flow in Laminar Flat-Plate Boundary Layer. 2006.
28. **Tauno Otto.** Models for Monitoring of Technological Processes and Production Systems. 2006.
29. **Maksim Antonov.** Assessment of Cermets Performance in Aggressive Media. 2006.
30. **Tatjana Barashkova.** Research of the Effect of Correlation at the Measurement of Alternating Voltage. 2006.
31. **Jaan Kers.** Recycling of Composite Plastics. 2006.
32. **Raivo Sell.** Model Based Mechatronic Systems Modeling Methodology in Conceptual Design Stage. 2007.
33. **Hans Rämml.** Experimental Methods for Sound Propagation Studies in Automotive Duct Systems. 2007.
34. **Meelis Pohlak.** Rapid Prototyping of Sheet Metal Components with Incremental Sheet Forming Technology. 2007.
35. **Priidu Peetsalu.** Microstructural Aspects of Thermal Sprayed WC-Co Coatings and Ni-Cr Coated Steels. 2007.
36. **Lauri Kollo.** Sinter/HIP Technology of TiC-Based Cermets. 2007.
37. **Andrei Dedov.** Assessment of Metal Condition and Remaining Life of In-service Power Plant Components Operating at High Temperature. 2007.
38. **Fjodor Sergejev.** Investigation of the Fatigue Mechanics Aspects of PM Hardmetals and Cermets. 2007.
39. **Eduard Ševtšenko.** Intelligent Decision Support System for the Network of Collaborative SME-s. 2007.
40. **Rünno Lumiste.** Networks and Innovation in Machinery and Electronics Industry and Enterprises (Estonian Case Studies). 2008.
41. **Kristo Karjust.** Integrated Product Development and Production Technology of Large Composite Plastic Products. 2008.
42. **Mart Saarna.** Fatigue Characteristics of PM Steels. 2008.
43. **Eduard Kimmari.** Exothermically Synthesized B₄C-Al Composites for Dry Sliding. 2008.
44. **Indrek Abiline.** Calibration Methods of Coating Thickness Gauges. 2008.
45. **Tiit Hindreus.** Synergy-Based Approach to Quality Assurance. 2009.
46. **Karl Raba.** Uncertainty Focused Product Improvement Models. 2009.
47. **Riho Tarbe.** Abrasive Impact Wear: Tester, Wear and Grindability Studies. 2009.
48. **Kristjan Juhani.** Reactive Sintered Chromium and Titanium Carbide-Based Cermets. 2009.

49. **Nadežda Dementjeva.** Energy Planning Model Analysis and Their Adaptability for Estonian Energy Sector. 2009.
50. **Igor Krupenski.** Numerical Simulation of Two-Phase Turbulent Flows in Ash Circulating Fluidized Bed. 2010.
51. **Aleksandr Hlebnikov.** The Analysis of Efficiency and Optimization of District Heating Networks in Estonia. 2010.
52. **Andres Petritšenko.** Vibration of Ladder Frames. 2010.
53. **Renee Joost.** Novel Methods for Hardmetal Production and Recycling. 2010.
54. **Andre Gregor.** Hard PVD Coatings for Tooling. 2010.
55. **Tõnu Roosaar.** Wear Performance of WC- and TiC-Based Ceramic-Metallic Composites. 2010.
56. **Alina Sivitski.** Sliding Wear of PVD Hard Coatings: Fatigue and Measurement Aspects. 2010.
57. **Sergei Kramanenko.** Fractal Approach for Multiple Project Management in Manufacturing Enterprises. 2010.
58. **Eduard Latõsov.** Model for the Analysis of Combined Heat and Power Production. 2011.
59. **Jürgen Riim.** Calibration Methods of Coating Thickness Standards. 2011.
60. **Andrei Surzhenkov.** Duplex Treatment of Steel Surface. 2011.
61. **Steffen Dahms.** Diffusion Welding of Different Materials. 2011.
62. **Birthe Matsi.** Research of Innovation Capacity Monitoring Methodology for Engineering Industry. 2011.
63. **Peeter Ross.** Data Sharing and Shared Workflow in Medical Imaging. 2011.
64. **Siim Link.** Reactivity of Woody and Herbaceous Biomass Chars. 2011.
65. **Kristjan Plamus.** The Impact of Oil Shale Calorific Value on CFB Boiler Thermal Efficiency and Environment. 2012.
66. **Aleksei Tšinjan.** Performance of Tool Materials in Blanking. 2012.
67. **Martinš Sarkans.** Synergy Deployment at Early Evaluation of Modularity of the Multi-Agent Production Systems. 2012.
68. **Sven Seiler.** Laboratory as a Service – A Holistic Framework for Remote and Virtual Labs. 2012.
69. **Tarmo Velsker.** Design Optimization of Steel and Glass Structures. 2012.
70. **Madis Tiik.** Access Rights and Organizational Management in Implementation of Estonian Electronic Health Record System. 2012.
71. **Marina Kostina.** Reliability Management of Manufacturing Processes in Machinery Enterprises. 2012.
72. **Robert Hudjakov.** Long-Range Navigation for Unmanned Off-Road Ground Vehicle. 2012.
73. **Arkadi Zikin.** Advanced Multiphase Tribo-Functional PTA Hardfacings. 2013.
74. **Alar Konist.** Environmental Aspects of Oil Shale Power Production. 2013.
75. **Inge Roos.** Methodology for Calculating CO₂ Emissions from Estonian Shale Oil Industry. 2013.

76. **Dmitri Shvarts.** Global 3D Map Merging Methods for Robot Navigation. 2013.
77. **Kaia Lõun.** Company's Strategy Based Formation of e-Workplace Performance in the Engineering Industry. 2013.
78. **Maido Hiimaa.** Motion Planner for Skid-Steer Unmanned Ground Vehicle. 2013.
79. **Dmitri Goljandin.** Disintegrator Milling System Development and Milling Technologies of Different Materials. 2013.
80. **Dmitri Aleksandrov.** Light-Weight Multicopter Structural Design for Energy Saving. 2013.
81. **Henrik Herranen.** Design Optimization of Smart Composite Structures with Embedded Devices. 2014.
82. **Heiki Tiikoja.** Experimental Acoustic Characterization of Automotive Inlet and Exhaust System. 2014.
83. **Jelena Priss.** High Temperature Corrosion and Abrasive Wear of Boiler Steels. 2014.
84. **Aare Aruniit.** Thermoreactive Polymer Composite with High Particulate Filler Content. 2014.
85. **Dmitri Gornostajev.** Development of the Calculation Method for Barge Hull. 2014.
86. **Liina Lind.** Wear of PVD Coatings on Fineblanking Punches. 2014.
87. **Nikolai Voltšihin.** Design and Technology of Oxides-Containing Ceramic-Based Composites. 2014.
88. **Aleksander Šablinski.** RANS Numerical Modelling of Turbulent Polydispersed Flows in CFB Freeboard. 2015.
89. **Tanel Aruväli.** Wireless Real-time Monitoring of Machining Processes. 2015.
90. **Andrei Bogatov.** Morphological Changes on Diamond and DLC Films During Sliding Wear. 2015.
91. **Raimo Kabral.** Aero-Acoustic Studies and Innovative Noise Control with Application to Modern Automotive Gas Exchange System. 2015.
92. **Jevgeni Sahno.** Dynamic Management Framework for Continuous Improvement of Production Processes. 2015.
93. **Ott Pabut.** Optimal Design of Slotless Permanent Magnet Generators. 2015.
94. **Merili Kukuškin.** Value Centric Business Development for Estonian Manufacturing Small and Medium Sized Enterprises. 2015.
95. **Kaimo Sonk.** Development of Additive Manufacturing Based on Functional Requirements. 2015.
96. **Marina Aghayan.** Functionalization of Alumina Nanofibers with Metal Oxides. 2016.
97. **Marek Jöeleht.** Titanium Carbide Cermet as Ballistic Protection Material. 2016.
98. **Heikki Sarjas.** Novel Synthesized and Milled Carbide-based Composite Powders for HVOF Spray. 2016.